Received: 25 April 2025 | Revised: 3 November 2025 | Accepted: 6 November 2025

DOI: 10.1002/pro.70390

RESEARCH ARTICLE

THE PROTEIN SOCIETY WILEY

Role of *N*-glycosylation as a determinant of ATG9A conformations and activity

Mattia Utichi[1,2] | **Matteo Lambrughi**[1] | **Henri-Baptiste Marjault**[1] | **Christian B. Borg**[1] | **Sergio Esteban Echeverría**[2] | **Kenji Maeda**[3] | **Nicholas M. I. Taylor**[4] | **Anders Gorm Pedersen**[5] | **Elisa Fadda**[6] | **Marja Jäättelä**[3] | **Elena Papaleo**[1,2]

[1]Cancer Structural Biology, Center for Autophagy, Recycling and Disease, Danish Cancer Institute, Copenhagen, Denmark

[2]Cancer Systems Biology, Section for Bioinformatics, Department of Health and Technology, Technical University of Denmark, Lyngby, Denmark

[3]Cell Death and Metabolism, Center for Autophagy, Recycling and Disease, Danish Cancer Institute, Copenhagen, Denmark

[4]Structural Biology of Molecular Machines Group, Protein Structure & Function Program, Novo Nordisk Foundation Center for Protein Research, ICMM, Faculty of Health and Medical Sciences, University of Copenhagen, Copenhagen, Denmark

[5]Section for Bioinformatics, Department of Health and Technology, Technical University of Denmark, Lyngby, Denmark

[6]School of Biological Sciences, University of Southampton, Southampton, UK

Correspondence
Elena Papaleo, Cancer Structural Biology, Center for Autophagy, Recycling and Disease, Danish Cancer Institute, Strandboulevarden 49, 2100, Copenhagen, Denmark.
Email: elenap@cancer.dk

Funding information
DECI-PRACE 17th; Danmarks Frie Forskningsfond, Grant/Award Number: 102517; Danmarks Grundforskningsfond, Grant/Award Number: DNRF125; EuroHPC, Grant/Award Numbers: EHPC-BEN-2023B02-010, EHPC-REG-2023R01-051; NovoNordisk Fonden, Grant/Award Numbers: NNF14CC0001, NNF20OC0065262, NNF23OC0081528

Review Editor: Lynn Kamerlin

Abstract

Here, we investigate the effects of glycosylation at position N99 on the structural dynamics and lipid scrambling activity of ATG9A, a key autophagy protein, using microsecond all-atom molecular dynamics simulations. ATG9A is an integral membrane protein involved in autophagosome biogenesis, and glycosylation at N99 has previously been implicated in intracellular trafficking, although its precise role remains unclear. The simulations reveal that the hydrophilic central cavity of ATG9A supports lipid reorientation and partial trans-bilayer movements, consistent with experiments on its lipid scrambling activity. We propose that N-glycosylation at N99 enhances cooperative interactions between protomers, facilitating lipid insertion and translocation within the central cavity. These findings suggest a mechanism by which glycosylation may influence lipid redistribution across the phagophore membrane during autophagy. To test this hypothesis, we generate N99 variants ($ATG9A^{N99A}$ and $ATG9A^{N99D}$) lacking N-glycosylation. These mutants show no significant changes in autophagy flux, suggesting that N99 glycosylation may not be essential for bulk autophagic processing. However, the analysis of autophagosome size indicates that the variants fail to rescue the enlarged vesicle phenotype of ATG9A-KO cells, unlike wild-type ATG9A. Thus, glycosylation might fine-tune ATG9A function, influencing vesicle morphology through conformational dynamics and lipid transport. We also observe asymmetric protomer conformations in ATG9A, in contrast to the symmetric structures obtained from cryo-EM, suggesting that structural heterogeneity could be further explored with experimental methods. Overall, our study highlights the importance of including glycosylation in computational models of membrane proteins and provides mechanistic insight into lipid transport during autophagy, with potential implications for other lipid scramblases and flippases.

KEYWORDS
ATG9A, autophagy, glycosylation, membranes, molecular dynamics, post-translational modifications

Mattia Utichi and Matteo Lambrughi contributed equally to this study.

1 | INTRODUCTION

Autophagy is a complex, evolutionarily conserved process through which cells degrade and recycle their components. This mechanism is essential for maintaining cellular homeostasis and responding to various cellular stresses (Yamamoto et al., 2023). Among the many post-translational modifications that modulate protein function, N-linked glycosylation (or N-glycosylation) plays a pivotal role in enhancing structural stability, protein folding, trafficking, and quality control (Reggiori et al., 2021). N-glycosylation has also been implicated in the regulation of autophagy, although its specific roles can vary across distinct autophagy pathways. For example, in chaperone-mediated autophagy (CMA), N-glycans are required for the function of the lysosomal membrane protein LAMP-2A, where they contribute to the protein's stabilization and multimeric complex formation at the lysosome (Eskelinen et al., 2003). While LAMP-2A operates within the CMA pathway, which is mechanistically and functionally distinct from macroautophagy (Bejarano & Cuervo, 2010), this example highlights the broader importance of glycosylation in regulating the activity of membrane-associated proteins involved in autophagic processes.

Similarly, ATG9A (UniProt Q7Z3C6), another N-glycosylated autophagic protein, plays an essential role in macroautophagy. It is critical for the autophagosome, the double membrane vesicle that engulfs cytoplasmic cargo and delivers it to lysosomes for degradation. Notably, ATG9A is the only integral membrane protein within the core autophagy machinery (Noda et al., 2009). During basal conditions, it traffics through the trans-Golgi network and endosomes (Young et al., 2006). Upon autophagy induction, ATG9A is mobilized to phagophore assembly sites, where it contributes to the biogenesis and expansion of the phagophore membrane (He et al., 2013; Kishi-Itakura et al., 2014; Popovic & Dikic, 2014; Puri et al., 2013; Sawa-Makarska et al., 2020; Takahashi et al., 2011).

ATG9A has been implicated in multiple stages of autophagosome formation, including phagophore initiation, elongation, and closure. It interacts not only with ATG2 proteins, which mediate lipid transfer from the ER, but also with the ULK1 kinase complex via ATG13 and ATG101, suggesting a broader regulatory role within the autophagy initiation machinery (Broadbent et al., 2023; Javed et al., 2025; Olivas et al., 2023). ATG9A interacts with ATG2 proteins, which are lipid transfer proteins (Maeda et al., 2019; Valverde et al., 2019; Wang et al., 2024) that form a heteromeric complex critical for phagophore biogenesis (Tang et al., 2019; van Vliet et al., 2022). The current evidence suggests that ATG2 proteins transfer lipids from the ER to the nascent phagophore. ATG9A, which has a lipid scrambling activity, redistributes lipids between the two leaflets of the phagophore membrane, enabling its elongation and the biogenesis of the autophagosome (Chumpen Ramirez et al., 2023; Guardia et al., 2020; Kotani et al., 2018; Maeda et al., 2020; Matoba et al., 2020; Matoba & Noda, 2020; Wang et al., 2024). Human ATG9A and yeast Atg9 share a homotrimeric structure with a unique fold and a complex network of branched cavities (Figure 1a,b) (Guardia et al., 2020; Maeda et al., 2020; Matoba et al., 2020). This network of cavities includes: (i) a central cavity whose interfaces are provided by each of the three protomers, (ii) a lateral cavity for each protomer, connecting the central cavity to the interface between the cytosolic leaflet of the membrane and the cytosol, and (iii) a perpendicular cavity for each protomer, connecting the lateral cavity to the cytosolic side of the protein (Figure 1a,b). These cavities can provide different routes for lipid transfer between the two membrane leaflets and may play a role in lipid scrambling.

Structural and molecular dynamics (MD) studies have revealed that ATG9A and its yeast homolog Atg9 are highly flexible within lipid membranes. Unlike the more rigid detergent-solubilized structures seen by cryo-EM (Matoba et al., 2020), simulations in lipid bilayers show dynamic protomer rearrangements driven by a hinge domain, narrowing the central pore and modulating lipid access (Chiduza et al., 2024; Matoba et al., 2020). In ATG9A, lipid headgroups spontaneously insert into the solvated central pore through transient openings at protomer interfaces, consistent with lipid scrambling activity (Maeda et al., 2020). ATG9A also induces local membrane curvature, which is amplified in clusters, suggesting it remodels autophagosome membranes via lipid-mediated effects rather than direct protein–protein interactions (Guardia et al., 2020). These findings support ATG9A as an energy-independent scramblase whose activity and membrane effects are structurally regulated, though potential modulation by post-translational modifications such as glycosylation remains unclear.

In vitro and in vivo experiments have demonstrated that human ATG9A is N-glycosylated exclusively at residue N99, making it the only occupied site among the four potential *N*-glycosylation sites (N99, N129, N224, and N507) in ATG9A (Staudt et al., 2016; Young et al., 2006). Earlier studies indicate that the glycan at N99 is complex (Young et al., 2006), which is compatible with the localization of the protein in the trans-Golgi.

It has been suggested that the N-glycosylation of ATG9A contributes to its subcellular trafficking (Staudt et al., 2016; Young et al., 2006). Deletion of the C-terminal region spanning residues 593–761 of ATG9A impairs its trafficking to the Golgi apparatus. Within this region, the LxM-type motif (residues 711–713) has been specifically implicated in transport from the endoplasmic reticulum to the Golgi, as mutations in this motif reduce the amount of ATG9A bearing

complex-type glycans. In contrast, an N-terminal deletion mutant lacking residues 233–252 shows reduced ATG2A binding and autophagy flux, while maintaining lipid-scrambling activity (van Vliet et al., 2022). Despite the absence of complex-type N-glycosylation, this mutant still localizes to the Golgi when stably expressed in cells. Together, these findings indicate that the C-terminal region of ATG9A is crucial for Golgi trafficking and glycan maturation at the N99 site, whereas the N-terminal region contributes to autophagy-related interactions without disrupting Golgi localization. This suggests that ATG9A trafficking and glycan processing may be regulated through distinct mechanisms. One hypothesis is that ATG9A may act as a reservoir, ready to be rapidly mobilized to its final localization in response to specific stimuli (Staudt et al., 2016; Young et al., 2006). Of note, the N99 glycosylation site is not conserved in yeast Atg9 (Orsi et al., 2012), highlighting potential

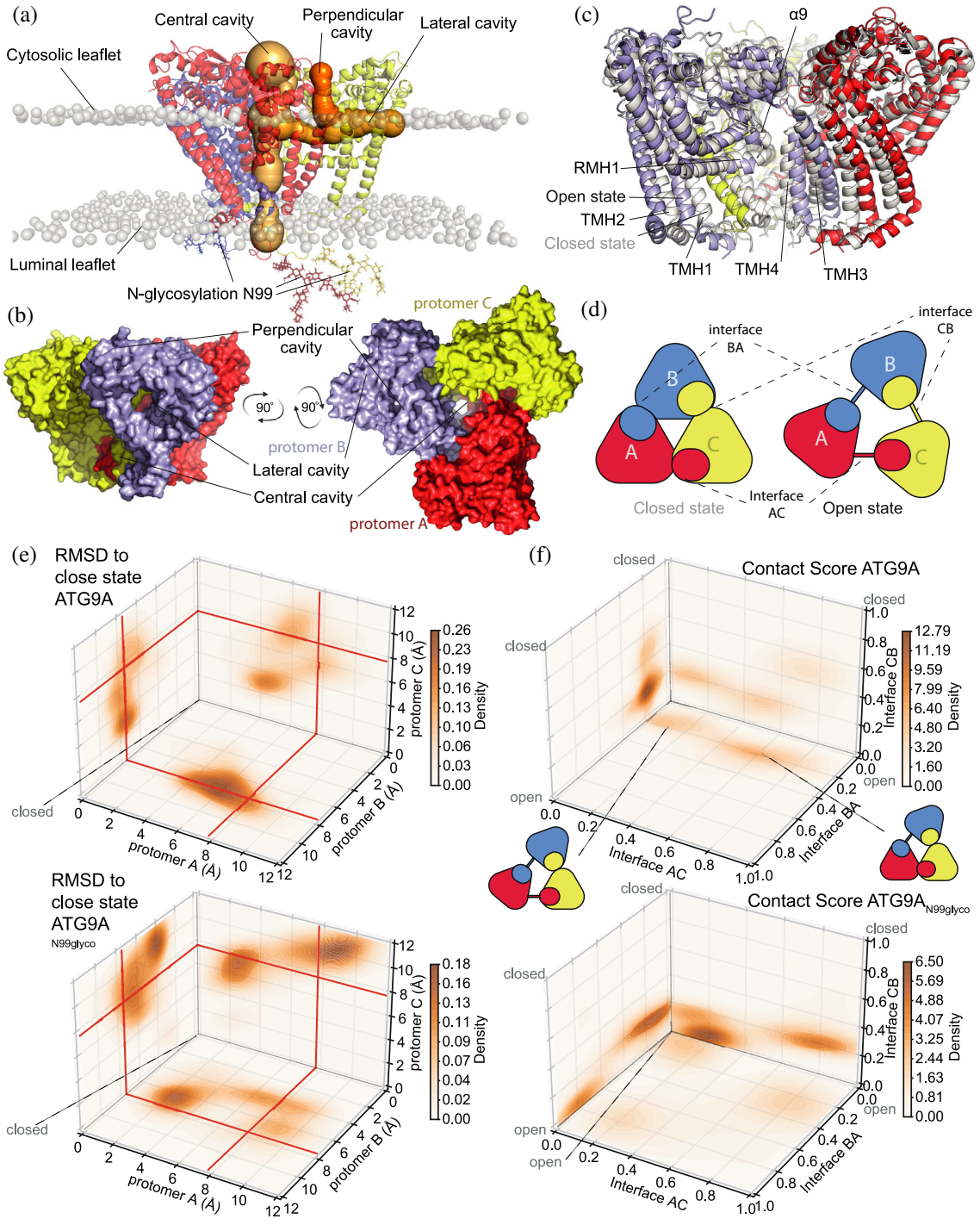

FIGURE 1 Legend on next page.

evolutionary divergence and suggesting that glycosylation may play a species-specific role in regulating human ATG9A function.

N99 is located in a short loop between the first and the second transmembrane helices (TMH1 and TMH2) of ATG9A. It is positioned near the luminal opening of the central cavity and faces the domain-swapped TMH3 and four helices (Figure 1a–c). This loop remains unresolved in the electron density from all currently available cryo-electron microscopy (cryo-EM) structures (Guardia et al., 2020; Maeda et al., 2020; Matoba et al., 2020). The precise role of *N*-glycosylation in modulating ATG9A structure, function and dynamics remains unclear. The complex architecture and inherent flexibility of glycans hamper their experimental characterization using structural biology techniques (Chau et al., 2023). Molecular Dynamics (MD) simulations, however, can offer valuable insights into the conformational ensembles of *N*-glycans and glycoproteins (Fadda, 2022). Prompted by these observations, we ran MD simulations of the ATG9A homotrimer in lipid bilayers to investigate the role of *N*-glycosylation at N99 on ATG9A protein dynamics and structure and disclose different mechanistic aspects. To assess possible functional effects, we also evaluated whether removal of the N-glycan alters autophagic activity using autophagy flux assays as a biological readout (Klionsky et al., 2021). These assays monitor the turnover of autophagy substrates such as LC3B-II and p62, which reflect the net activity of the autophagy pathway. Thus, alterations observed in these assays may reflect effects on different stages of the pathway rather than a specific mechanistic step. We used glycosylation-null mutants of ATG9A ($ATG9A^{N99A}$ and $ATG9A^{N99D}$) to explore the impact of N-glycosylation on autophagic function in a cellular context. Beyond flux assays, we also analyzed autophagosome size in ATG9A knockout (KO) cells. This analysis was guided by previous findings that ATG9A KO cells display enlarged autophagosomes compared to cells expressing wild-type ATG9A (Runwal et al., 2019), highlighting a role for ATG9A in maintaining autophagosome morphology. By comparing autophagosome size across wild-type, KO, and glycosylation-null conditions, we aimed to determine whether N-glycosylation at position N99 contributes to proper autophagosome formation and structural regulation during autophagy.

2 | RESULTS

2.1 | ATG9A undergoes asymmetric closed-open conformational changes in the non-glycosylated and glycosylated state

The ATG9A loop, which includes the N-glycosylated residue N99, is positioned at the interface between the solvent and the lipid headgroups of the membrane, close to the luminal opening of the protein's central cavity (Figure 1a). This positioning prompted us to investigate whether *N*-glycosylation of N99 modulates the conformational states of ATG9A. To this end, we ran 1 μs-long MD trajectories by conventional (deterministic) sampling of the homotrimeric ATG9A (residues 36–522) in both its N-glycosylated ($ATG9A_{N99glyco}$) and non-glycosylated forms (ATG9A) (Table 1), embedded

FIGURE 1 ATG9A homotrimer undergoes asymmetric closed-open conformational changes in the non-glycosylated and glycosylated state. (a) Starting model for MD simulations of *N*-glycosylated ATG9A homotrimer ($ATG9A_{N99glyco}$). ATG9A is depicted as a cartoon representation, highlighting its three distinct protomers A (red), B (blue) and C (yellow). ATG9A has a complex network of branched cavities, including a shared central cavity and individual lateral and perpendicular cavities for each protomer. For protomer C, the radius of the internal cavities is visualized as orange spheres. The N99 *N*-glycosylation are represented as sticks. The lipid headgroups of the lipid bilayer are shown as gray spheres. (b) Surface representation of ATG9A homotrimer in the closed state shown from the side and top in the left panel and right panel, respectively. The network of cavities is shown and the protomers A, B, and C are highlighted in red, blue, and yellow. (c) Cryo-EM structures of ATG9A as cartoon representation, showing two distinct symmetric conformations of ATG9A protomers denoted as open (PDB ID: 6WQZ) and closed (PDB ID: 7JLP) states. In the open state, the protomers A, B, and C are colored red, blue, and yellow, whereas in the closed state, they are represented in white. These conformations are characterized by the different distance between the domain-swapped transmembrane helices (TMH3-4) and the reentrant membrane helix 1 (RMH1)-turn-helix α9, as well as the rest of the protomer and the TMH3–4 helices of adjacent protomers. (d) Schematic representation showing the open and closed symmetric conformations of ATG9A at the domain-swapped interfaces between the protomers (specifically at the AC, BA, and CB interfaces, named after the involved protomers). (e) Root Mean Square Deviation (RMSD) of the Cα atoms in the domain-swapped transmembrane helices of each protomer of ATG9A (upper panel) and $ATG9A_{N99glyco}$ (lower panel) in relation to the experimental cryo-EM closed state for ATG9A. Both alignment and RMSD calculations were performed on the Cα atoms of the domain-swapped transmembrane helices, as described in the Methods section. RMSD values were computed for each frame of the concatenated 3-μs trajectories ($n = 3000$ frames, sampled every 1000 ps). The plots show the bi-dimensional density projections of RMSD values calculated for the concatenated trajectories. For context, the RMSD between the closed and open state is around 7.8 Å, highlighted by red lines in the plots. Starting from the closed-state conformation, both ATG9A and $ATG9A_{N99glyco}$ exhibit conformational changes towards the open state in at least one protomer. (f) Contact score values calculated for ATG9A (upper panel) and $ATG9A_{N99glyco}$ (lower panel). The contact score quantifies the occurrence of protein–protein contacts between the domain-swapped TMH3-4 domains of each protomer and other regions of ATG9A that are present only in the cryo-EM structure of the closed state. A score of 1 indicates a close resemblance to the closed state. The plots show the bi-dimensional density projections of the contact score values of each protomer interface (AC, BA, and CB) calculated for the concatenated 3-μs trajectories($n = 3000$ frames, 1000 ps timestep). Both ATG9A and $ATG9A_{N99glyco}$ assume asymmetric open states of the protomers, with the closed-to-open conformational changes driven by the separation of the domain-swapped interfaces of the protomers.

TABLE 1 Summary of the collected simulations.

System	Force Field	Lipid bilayer composition	Total atoms	Lenght time (μs)	N° replicates
ATG9A	CHARMM36m	POPC 75% CHOL 25%	323,637	1	3
$ATG9A_{N99glyco}$	CHARMM36m	POPC 75% CHOL 25%	354,144	1	3

in a lipid bilayer composed of 1-palmitoyl-2-oleoyl-sn-glycerol-3-phosphocholine (POPC) and cholesterol (Figure 1a,b).

Because a single unbiased MD trajectory is likely to sample only a limited portion of the conformational space, we concatenated the ATG9A and $ATG9A_{N99glyco}$ trajectories into two 3 μs macro-trajectories and analyzed these, along with the single replicates, to improve sampling and capture a broader range of conformational states.

Cryo-EM data show that ATG9A protomers (named protomer A, B and C) can adopt two distinct conformations, referred to as "open" and "closed" states in the regions surrounding the central cavity (Figure 1c,d) (Guardia et al., 2020; Maeda et al., 2020; Matoba et al., 2020). These conformations are defined by the degree of separation between the domain-swapped transmembrane helices (TMH3-4) and the rest of the same protomer as well as the TMH3–4 helices of the neighboring protomers at the interfaces (AC, BA, and CB, named after the interacting protomers, Figure 1d). In the open state, this separation is larger, while in the closed state, it is smaller.

We monitored two different parameters to characterize transitions between the closed and open states of ATG9A and $ATG9A_{N99glyco}$, namely the Root Mean Square Deviation (RMSD) of the Cα atoms of the domain-swapped transmembrane helices of each protomer (TMH3-4) relative to the closed experimental cryo-EM structures (Figures 1e and S1 and S2) and a contact score based on the occurrence of protein–protein contacts among the TMH3–4 helices of each protomer and other regions of ATG9A that are present only in the cryo-EM structure of the closed state (Figures 1f and S3). We observed that in both ATG9A and $ATG9A_{N99glyco}$, at least one protomer spontaneously transitioned towards the open state when starting from a closed state (Figures 1e,f and S1). The asymmetric open states of the protomers obtained from the MD simulations (Figure 1e,f) do not fully capture the complete open state observed in the cryo-EM data, which consistently shows a symmetric orientation of the protomers in all ATG9A structures (Guardia et al., 2020; Maeda et al., 2020). This suggests the presence of a high energy barrier that prevents reaching the fully open state during the simulations. Further analysis of the cryo-EM data for ATG9A pointed out that the high-resolution structure determination in a nanodisc environment (PDB ID 7JLP, resolution 3.4 Å) (Maeda et al., 2020) was based on approximately only 2.4% of the initial particle images. Similarly, the highest resolution structures of ATG9A in detergent for the open (PDB ID: 6WQZ, resolution 2.8 Å) and closed (PDB ID: 6WR4, resolution 2.9 Å) states (Guardia et al., 2020) were derived from processing only 8.5% and 9.3% of the initial 2D particle images, respectively. These observations suggest that the available cryo-EM data may not fully rule out the existence of structural heterogeneity and additional conformational states beyond the reported open and closed configurations. This raises the possibility that certain states within the cryo-EM data could reflect the asymmetric conformations observed in the MD simulations.

To better quantify this behavior, we calculated the RMSD of TMH3–4 for each protomer relative to the closed cryo-EM structure across the 3-μs trajectories (Figure S4). This additional analysis confirms that transitions occur asynchronously: for example, when protomer A adopts a more open-like state, protomers B and C remain in closed conformations, thereby providing further evidence of asymmetry.

The closed-to-open conformational changes in the MD trajectories are driven by the separation of the domain-swapped interfaces of the protomers (Figure 1e,f), resulting in a lateral opening of the central cavity towards the hydrophobic portion of the lipid bilayer. These data align with findings from cryo-EM data and from previous all-atom MD simulations (Maeda et al., 2020). The opening of the domain-swapped interfaces involves interactions between the reentrant membrane helix 1 (RMH1)-turn-helix α9 of each protomer and TMH3–4 (Figure 1c,d). This behavior is evident in replicate 1 of $ATG9A_{N99glyco}$, where all three domain-swapped interfaces shifted closer to the open state (Figures S1 and S3). Conversely, we also observed states in $ATG9A_{N99glyco}$ with a high occurrence of specific contacts (i.e., contact score values close to 1), indicating that closed conformations are preserved in certain regions (Figure 1f). For example, this is reflected in the interface BA of replicate 2 and interface AC of replicate 3 in $ATG9A_{N99glyco}$ (Figure S3). Additionally, both ATG9A and $ATG9A_{N99glyco}$ can adopt conformations with high RMSD relative to both the experimental close and open structures. This is exemplified by the interface CB in replicate 2 of $ATG9A_{N99glyco}$, (Figures 1e and S2). These conformations provide alternative orientations of

the TMH3–4 helices that are different from those observed in the final cryo-EM models (Guardia et al., 2020; Maeda et al., 2020; Matoba et al., 2020).

2.2 | N-glycosylation at N99 favors the extent of open conformations in ATG9A

We performed clustering of trajectory frames based on contact scores at the domain-swapped protomer interfaces. We used Euclidean distance, while accounting for ATG9A's threefold symmetry (i.e., interfaces AC, BA and CB), to gain deeper insights into the protein dynamics and identified diverse conformational states sampled by ATG9A and ATG9A$_{N99glyco}$ (Figures 2 and 3). A quality-threshold clustering approach (Heyer et al., 1999) (threshold 0.45) was applied, discarding clusters with fewer than 60 frames, and representative structures were identified based on minimal mean square distance within each cluster. In our MD simulations, cluster analysis and examination of representative structures unveiled different open and closed states in glycosylated ATG9A that are not at all or only rarely observed in non-glycosylated ATG9A and vice versa (Figure 2a,b and Table S1). To compare ATG9A and ATG9A$_{N99glyco}$, we calculated Jaccard and weighted Jaccard similarity scores to quantify differences in contact score distributions (Figure 2c and Table S1). Further structural stratification was conducted using kernel density analysis of RMSD values for transmembrane TMH3-4 helices, referencing experimental cryo-EM structures of the open and closed states. ATG9A$_{N99glyco}$ exhibited a higher occurrence of open conformations at all protomer interfaces compared to ATG9A. These open states were predominantly found in cluster 2 of ATG9A$_{N99glyco}$, which encompassed approximately 30% of the concatenated trajectory frames. This cluster displayed representative contact scores of 0.2, 0.05, and 0.15 for interfaces AC, BA, and CB, respectively (Figure 2b). In contrast, ATG9A displayed only a partial population of such open states. Specifically, cluster 1 (comprising around 56% of the concatenated trajectory frames) (Figure 2a) and cluster 5 (representing around 2% of the frames) showed limited similarity with cluster 2 of ATG9A$_{N99glyco}$, as indicated by the low Jaccard similarity values of approximately 15% and 10%, respectively (Figure 2c and Table S1). Cluster 1 of ATG9A included partially open and asymmetric states, with average contact scores of 0.35, 0.2, and 0.15 for the AC, BA, and CB interfaces, respectively, indicating a more closed conformation of the interfaces (Figure 2a). Similar asymmetric states, characterized by one or two open interfaces while the others remained closed, were observed in clusters 1, 3, 4, 6, and 7 of ATG9A$_{N99glyco}$ and clusters 2, 3, and 4 of ATG9A. ATG9A$_{N99glyco}$ exhibited a higher frequency of states involving at least one interface with a particularly high contact score (above 0.5), particularly in clusters 1 and 5 (Figures 2b and 3). In contrast, these states were less common in ATG9A and appeared in clusters 2, 3, and 4, showing limited overlap with clusters 1 and 3 of ATG9A$_{N99glyco}$ (Figure 2c and Table S1). The presence of these closed states at domain-swapped interfaces might be influenced by the initial structure or be intermediate states during closed-open conformational changes. We thus further analyzed the individual replicates by examining collective contact scores and the RMSD of domain-swapped interfaces relative to the experimental cryo-EM structures (Figure S5). While open conformational states were observed across replicates, there were distinct differences in their sampling behavior. Replicate 1 of ATG9A$_{N99glyco}$ predominantly sampled open states for all three protomers, whereas replicates 2 and 3 primarily sampled conformations with two open interfaces and one closed interface (BA and AC, respectively). Further analysis of these states suggested that the ability of ATG9A$_{N99glyco}$ to maintain closed domain-swapped interfaces could be linked to interactions between *N*-glycans and the luminal loops of neighboring protomers. Investigation of the surrounding environment of the three N-glycosylation revealed heterogeneous and transient interactions with glycan, protein, and lipid atoms (Figures S6 and S7). Moreover, in the second half of replicate 2, we observed an increased presence of protein and lipid atoms near the *N*-glycan of protomers C and B. These interactions may play a role in modulating the open or closed states of the domain-swapped interfaces.

Overall, our MD simulations suggested that the glycosylation of N99 favored the extent of open conformations. The occurrence of closed conformations in ATG9A$_{N99glyco}$ associated with interactions between *N*-glycans from different protomers during the simulation should be taken cautiously, as inherent force-field limitations might influence them (Fadda, 2022).

2.3 | N99 glycosylation promotes cooperativity in the conformational changes of ATG9A

The analysis of the contact score presented above enabled us to discriminate between closed and open conformations of the individual ATG9A protomers relative to the cryo-EM reference states. Cooperativity in conformational changes is a hallmark of oligomeric proteins, playing a critical role in their functional modulation (Liu & Luo, 2023; Umeki et al., 2016). To investigate this aspect, we employed a statistical framework to explore the relationships among the open/closed states of each protomer (A, B, and C) of ATG9A and ATG9A$_{N99glyco}$ with the open/closed state of the other protomers. Our goal was to evaluate if cooperativity played a role in the closed-to-open conformational

change and in the effects of the *N*-glycosylation on this mechanism.

We used Log-Linear Models (LLMs) with the Poisson family to fit the contact score data and calculate deviance and log-likelihood (Figures 4a and S8). These models are well-suited for modeling relationships among categorical variables, effectively capturing the complex interplay and dependencies between the protomer states. To evaluate the performances of different LLMs, we applied chi-squared statistics and calculated deviance and log-likelihood (Figure S8).

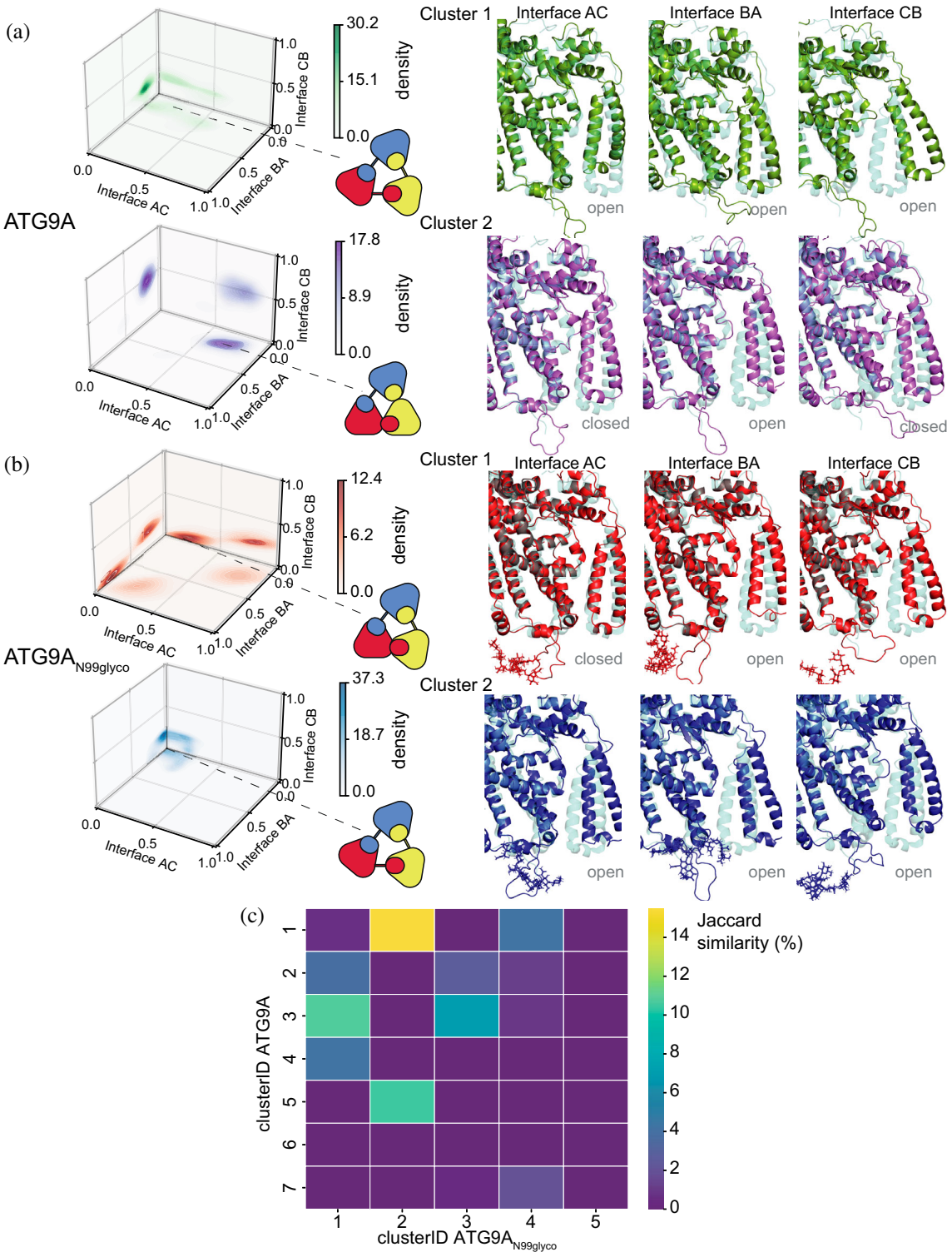

FIGURE 2 Legend on next page.

For both ATG9A and ATG9A$_{N99glyco}$, the complete independence model ([A, B, C]) exhibited higher deviance and lower log-likelihood, indicating a poor fit and suggesting dependencies in the open/closed states among the protomers (Figures 4a and S8). In ATG9A, both the homogeneous association model ([AB, AC, BC]) and conditional independence models, particularly [AC, BC] and [AB, AC], resulted in low deviances and high log-likelihoods. These findings suggest potential dependencies among the open/closed states of all protomers, or a scenario where the status of two protomers (A, B and B, C) is influenced by the status of the third (C and A, respectively).

Comparatively, ATG9A$_{N99glyco}$ displayed a distinct relationship in protomer open/closed states. The joint dependence ([A, BC], [B, AC], [C, AB]), and conditional independence models did not show a better fit than the complete independence model (Figures 4a and S8). Notably, for ATG9A$_{N99glyco}$ the homogeneous association model ([AB, AC, BC]) provided the best fit for the contact score data, with the lowest deviance and highest log-likelihood among all models. This suggests a dependent relationship among all three protomers, with their open/closed states collectively influenced, an effect less apparent in ATG9A. Overall, our results provide a model in which glycosylation at

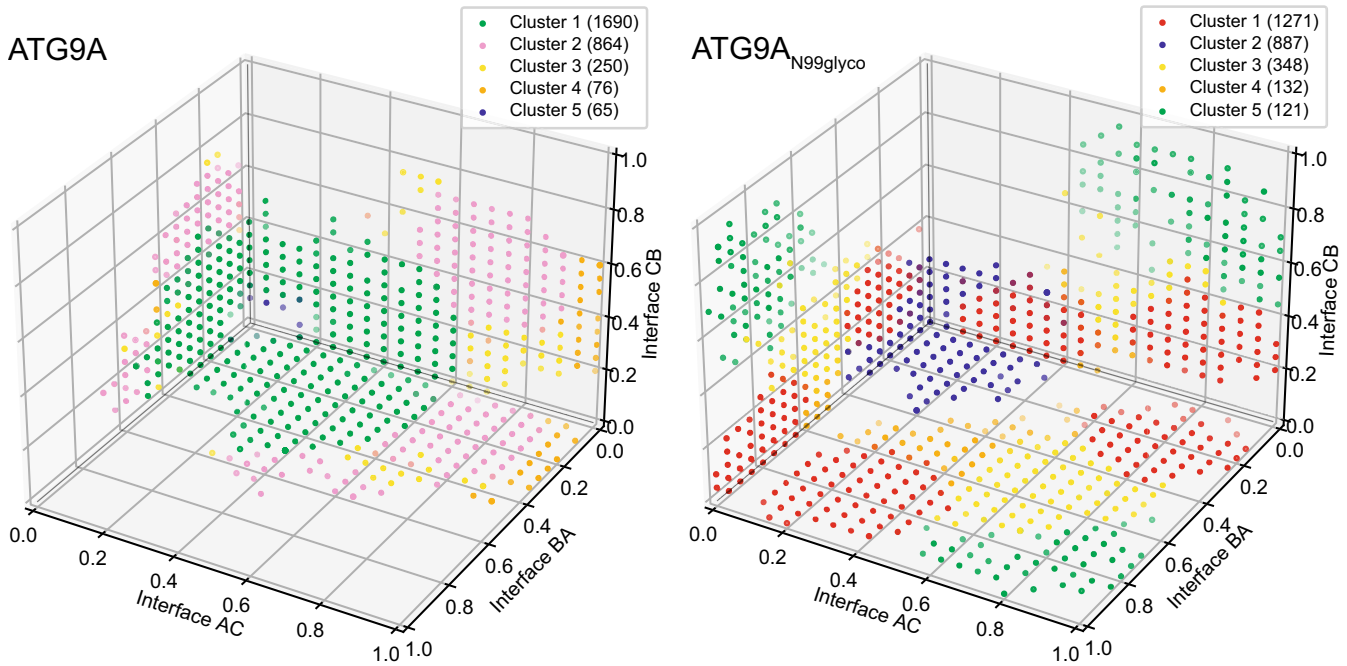

FIGURE 3 N-glycosylation at N99 favors the extent of open conformations in ATG9A. The three-dimensional plots show the results of the cluster analysis calculated on the concatenated 3-μs trajectories of ATG9A and ATG9A$_{N99glyco}$ ($n = 3000$ frames, 1000 ps timestep) using the Euclidean distance metric based on the contact scores of each protomer-protomer interface AC, BA, and CB. A quality-threshold algorithm was employed with a threshold of 0.45, discarding clusters with <60 frames (<2% of the total). Each dot represents a structure from the concatenated trajectories colored according to the cluster ID. Cluster 1 of ATG9A included partially open states, including around 56% of the concatenated trajectory frames. ATG9A$_{N99glyco}$ exhibits a higher occurrence than ATG9A of states with open conformations at all protomer interfaces, as represented by cluster 2, encompassing around 30% of the concatenated trajectory frames.

FIGURE 2 N-glycosylation at N99 modulates open-closed states of ATG9A homotrimer. The cluster analysis was conducted on the concatenated 3-μs trajectories of ATG9A (a) and ATG9A$_{N99glyco}$ (b) ($n = 3000$ frames, 1000 ps timestep). The analysis employed an Euclidean distance metric based on the contact scores at each protomer–protomer interface (interfaces AC, BA, and CB). A quality-threshold algorithm was employed with a set threshold of 0.45. The left panels display the bi-dimensional density projections of the contact score values for the two main clusters of ATG9A (a) and ATG9A$_{N99glyco}$ (b). The right panels provide detailed highlights of the AC, BA and CB interfaces for the representative structures from the first and second main clusters identified. The structures are depicted using a cartoon model, and for reference purposes, they are superimposed on the closed-state structure, which is illustrated as a blue, semi-transparent cartoon. The N99 *N*-glycosylation are represented as sticks. (c) Heatmap of the Jaccard similarity index, calculated to evaluate the occurrence and commonality of states within each identified cluster for ATG9A and ATG9A$_{N99glyco}$. A Jaccard similarity index value of 100% indicates identical state sets, while 0% indicates no similarity. ATG9A$_{N99glyco}$ shows a higher occurrence than ATG9A of states with open conformations at all protomer interfaces (as seen in cluster 2, characterized by representative contact scores of 0.2, 0.05, and 0.15 for interfaces AC, BA, and CB). ATG9A only partially populates such open states (in cluster 1 and cluster 5), showing low similarity with cluster 2 of ATG9A$_{N99glyco}$. ATG9A and ATG9A$_{N99glyco}$ in cluster 1 are asymmetric states, characterized by either two or one open interfaces, while the remaining interfaces are in a closed state.

N99 enhances cooperative interactions among the protomers, potentially modulating the closed-open conformational changes.

Building on these results, we further analyzed the open and closed states of individual protomers to evaluate the existence of alternative conformations not captured in the deposited cryo-EM structures. To this end, we performed RMSD calculations for the domain-swapped regions of each protomer relative to the experimental cryo-EM structures (Figure 4b). The classification of protomer states was based on structural comparisons. If the RMSD between a given protomer conformation and the reference open or closed structure exceeded 7.8 Å, it was considered a distinct state. This threshold was chosen based on observed differences between open and closed cryo-EM structures.

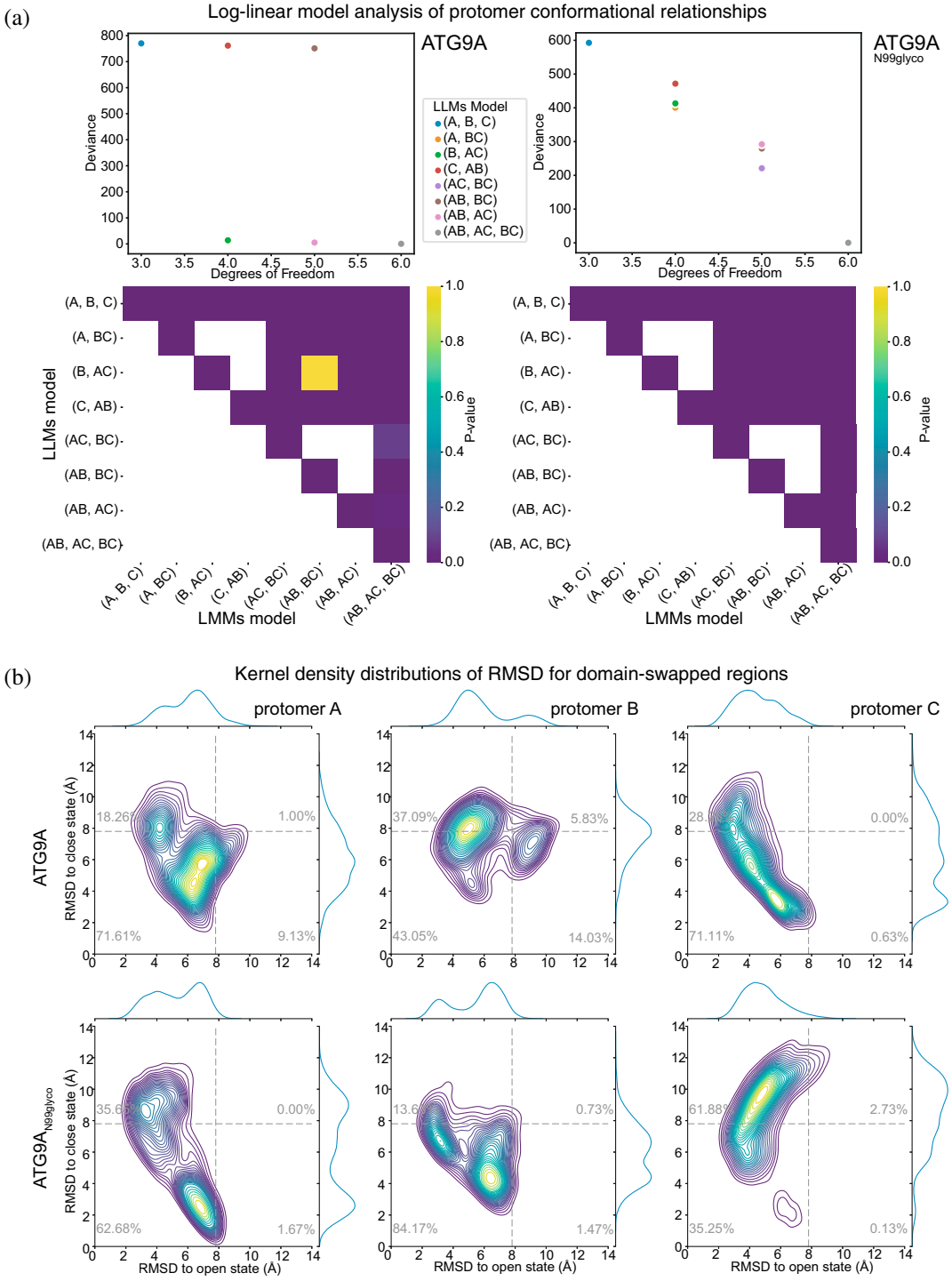

FIGURE 4 Legend on next page.

ATG9A$_{N99glyco}$ exhibited a higher occurrence of open-like states at the protomer interfaces (36%, 14%, and 62% for interfaces AC, BA, and CB, respectively) compared to ATG9A (18%, 37%, and 28%) (Figure 4b). Conversely, ATG9A showed a higher occurrence of alternative states with high RMSD values relative to both open and closed experimental structures (1%, 6%, 0% for interfaces AC, BA, and CB, respectively) than ATG9A$_{N99glyco}$ (0%, 0%, and 2%). This difference became more pronounced for ATG9A when considering states with RMSD values in the 6–8 Å range (Figure 4b). These findings suggest that *N*-glycosylation at N99 may contribute to restricting the conformational flexibility of ATG9A, limiting the occurrence of alternative states that deviate from the known open and closed experimental structures.

2.4 | Conformational changes modulate the shape and lipid accessibility of the central cavity of ATG9A

The different conformational states observed in ATG9A and ATG9A$_{N99glyco}$ may influence the protein internal cavities and their role in modulating lipid movements. To investigate these differences, we analyzed the internal cavities of ATG9A, specifically focusing on variations in cavity profiles between the open and closed states. Our analysis targeted the shape (i.e., radius and length) and accessibility of the central cavity formed by the three protomers (Figure 5), as this cavity is proposed to mediate lipid scrambling between membrane leaflets (Guardia et al., 2020; Maeda et al., 2020; Matoba et al., 2020). We carried out a similar analysis on the cryo-EM-derived models of the open and closed states for reference (Figure 5a). Consistent with previous findings (Guardia et al., 2020; Maeda et al., 2020), our analysis of the two reference structures revealed that the central pore is predominantly hydrophilic, highly solvated and spans approximately 60 Å.

The central cavity is constrained at the cytosolic entrance by helices α11 and α13 and, at the luminal side, by a hydrophobic gate at its narrowest point (cavity radius ~2.5 Å in the closed state) formed by TMH3-4 and helix α12. The luminal opening of the central cavity is further modulated by the luminal loop, which includes the *N*-glycosylation site, and the helices α2 and α3 (Figure 5a). The main difference between the open and closed states of ATG9A lies in the increased degree of cavity opening in the luminal region with the hydrophobic gate radius expanding to ~5.5 Å in the open state (Figure 5a). In both the open and closed structures, we identified three groups of side cavities adjacent to the central cavity. Each group corresponds to a domain-swapped interface and extends beneath α11 on the cytosolic side of the protein (Figure 5a). Lipid molecules were observed inserting their headgroups into these cavities in one of the available cryo-EM structures (Maeda et al., 2020).

We further examined the central cavity and each cluster in ATG9A and ATG9A$_{N99glyco}$ (Figure 5) from our cluster analysis. We calculated average profiles of the radius and length of the cavities across all frames within each cluster (Figure 5b,c). In the open states sampled by ATG9A$_{N99glyco}$, particularly cluster 2 (encompassing ~30% of the frames), the central cavity exhibited an average radius and length profile closely matching the reference open state (Figure 5b). Additionally, our analysis identified shorter cavities branching sideways from the central cavity at each domain-swapped interface, extending beneath RMH1-turn-helix α9 and TMH3–4 towards the hydrophobic bilayer environment (Figure 5b). In contrast, for ATG9A, cluster 2 states with two closed interfaces (AC and CB), showed an average central cavity profile resembling the reference closed state with a radius of ~3.5 Å around the hydrophobic gate (Figure 5c). In addition, the central cavity at the interface BA, which adopted open states, exhibited a sidewise opening (Figure 5c, right panel).

FIGURE 4 N-glycosylation promotes cooperativity in the closed-open conformational changes of ATG9A (A) Log-Linear Models (LLMs) analysis illustrating the relationships among open/closed states of the protomers (A–C) of ATG9A (left panels) and ATG9A$_{N99glyco}$ (right panels) calculated on the combined 3-μs trajectories ($n = 3000$ frames, 1000 ps timestep). The upper panels show the degrees of freedom for the different LLMs and their deviance in fitting the contact score data, highlighting differences in the fit of independence models between ATG9A and ATG9A$_{N99glyco}$. We tested complete independence ([A, B, C]), joint dependence ([A, BC], [B, AC], [C, AB]), conditional independence ([AC, BC], [AB, BC], [AB, AC]) and homogeneous association model (i.e., [AB, AC, BC]). The lower panels show the p-value calculated as heatmaps to assess the significance of the deviance between different models. A low *p*-value (i.e., 0.05) suggests that the difference in deviance between the two compared models is statistically significant, that is, unlikely to have occurred by chance. The homogeneous association model (i.e., [AB, AC, BC]) showed a good fit of the contact score data of ATG9A$_{N99glyco}$, with the lowest deviance and highest log-likelihood (Figure S8) across all models, suggesting a dependent relationship among all three protomers, which is less apparent in ATG9A. (B) Kernel density distribution plots of the Root-Mean-Square Deviation (RMSD) values of domain-swapped regions for each protomer (A left panels, B middle panels, C right panels) relative to the cryo-EM closed and open structures. The analysis has been performed on the concatenated 3-μs trajectories of ATG9A (upper panels) and ATG9A$_{N99glyco}$ (lower panels) ($n = 3000$ frames, 1000 ps timestep). The dotted gray lines indicate the 7.8 Å threshold for RMSD values, calculated from comparing open and closed cryo-EM structures. ATG9A exhibited a higher occurrence of alternative states with high RMSD values relative to both open and closed experimental structures (1%, 6%, and 0% for interfaces AC, BA, and CB, respectively), compared to ATG9A$_{N99glyco}$ (0%, 0%, and 2%).

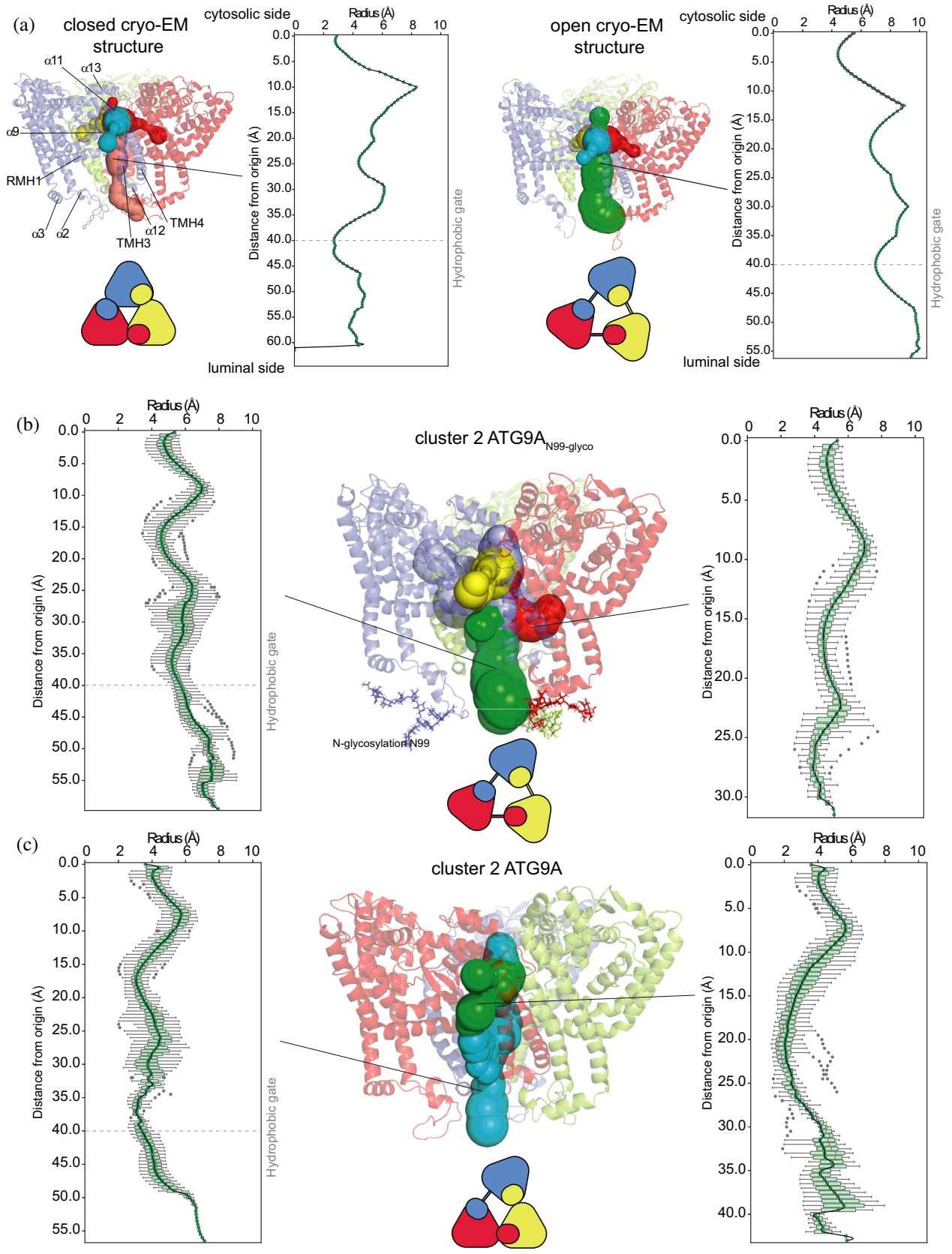

FIGURE 5 Legend on next page.

In addition to the central cavity, the CAVER analysis highlighted the presence of lateral and perpendicular cavities at the domain-swapped interfaces. These openings extended beneath RMH1–α9 and TMH3–4 towards the lipid bilayer, consistent with previously described lipid-binding sites in cryo-EM structures. In $ATG9A_{N99glyco}$, such lateral cavities were more frequently observed and reached larger radii in open clusters (particularly cluster 2), suggesting enhanced accessibility compared to ATG9A.

In the proposed model for ATG9A scrambling activity, the central cavity facilitates the trans-bilayer movement of phospholipids, with lipid molecules inserting into the cavity in both cryo-EM studies and MD simulations (Maeda et al., 2020). To further investigate the role of the N99 glycosylation in this mechanism, we monitored the entrance of phospholipids into the central cavity of ATG9A and their subsequent trans-bilayer movements.

We analyzed the evolution of the shape of the bilayer surface during the simulations and the lipid headgroup positions and their interactions with the protein using LipidDyn (Scrima et al., 2022). Lipids that reduced their distance to the opposite leaflet by at least 20% compared to the reference distance between the cytosolic and luminal leaflets were classified as undergoing partial translocation across the bilayer (Figure 6a). In $ATG9A_{N99glyco}$, a higher average of phospholipids exhibited trans-bilayer movements compared to ATG9A (34 vs. 27 phospholipids, respectively) (Figure 6a). A Bayesian binomial model estimated a 93% posterior probability that glycosylation increases the likelihood of POPC lipids traversing the membrane (Figure 6b).

Additionally, we investigated cholesterol translocation and observed that cholesterol molecules underwent trans-bilayer movements almost five times more frequently than phospholipids. However, no differences were detected between ATG9A and $ATG9A_{N99glyco}$ in terms of cholesterol translocation (Table S2).

Our simulations revealed that phospholipids from the luminal leaflet inserted their hydrophilic headgroups into the protein central cavity at the domain-swapped interfaces, orienting horizontally while their acyl tails remained within the bilayer hydrophobic environment (Figure 6c). Multiple phospholipids inserted at the same time into the central cavity and exhibited partial trans-bilayer motions (Figure 6d). Specifically, phospholipids from the luminal leaflet traversed ~60% of the distance between the luminal and cytosolic leaflets, reaching the region of RMH1 and TMH3–4 in each protomer (Figure 6c,d). Although additional simulations with enhanced sampling approaches would be necessary to observe complete trans-bilayer lipid movements, our findings suggest that this region may act as a gate or exit point for lipid movements.

In conclusion, our computational analyses point out a mechanism in which closed-to-open conformational changes resulted in sidewise openings and increased accessibility of the central cavity towards the hydrophobic region of the lipid bilayer. Additionally, the hydrophilic nature of the central cavity provides a favorable environment for the polar headgroups of phospholipids (Figure 6c,d). Open conformations of the protein facilitate lipid insertion into the central cavity, along with their reorientation and partial transbilayer movements, representing potential steps in the lipid scrambling mechanism. Furthermore, the wider radius of the central cavity in the open state (Figure 5b) allows it to accommodate the headgroups of diverse phospholipids, aligning with findings from scrambling assays (Maeda et al., 2020). N99 glycosylation overall facilitates the trans-bilayer movements.

2.5 | Autophagy flux analysis of ATG9A N99 variants

To complement the computational analyses, we next asked whether the predicted effects of N99 glycosylation on ATG9A dynamics and lipid accessibility would translate into measurable changes in protein function in cells. We therefore assessed autophagy flux as a functional readout (Tanida et al., 2005). The autophagic flux can be evaluated by measuring the turnover of key autophagy markers like LC3-II and SQSTM1/p62 under conditions that block lysosomal degradation, such as treatment with Bafilomycin A1 (Germain et al., 2011; Mizushima & Yoshimori, 2007). This approach distinguishes between autophagosome synthesis and degradation

FIGURE 5 Closed-open conformational changes of ATG9A modulate the radius and solvent accessibility of the central cavity of ATG9A. Analysis using CAVER of the radius and length of the central cavity and its side cavities. (a) Analysis of the cavities of the cryo-EM-derived models of the closed (left panels) and open (right panels) states. (b, c) Analysis of the cavities of cluster 2 of $ATG9A_{N99glyco}$ (b) and ATG9A (c), obtained from the MD simulations. The analysis was performed using CAVER on 20 representative frames extracted from the concatenated 3-μs trajectories ($n = 3000$ frames sampled every 1000 ps). The box plots show the average profiles of radius and length (calculated as the distance from the starting point for the cavity calculation) for the central cavities calculated across all the structures within each cluster. The ATG9A structure is shown as a cartoon, highlighting its three protomers: A (red), B (blue), and C (yellow). The cavities identified are represented as spheres colored based on the tunnel clusters. Each panel includes a schematic representation showing the open and closed asymmetric conformations of ATG9A at the protomer interfaces. The average profile of the central cavity from cluster 2 of $ATG9A_{N99glyco}$ is similar to the reference open state, showing shorter cavities that open sideways at each domain-swapped interface towards the hydrophobic environment of the bilayer.

(a)

POPC lipids exhibiting partial trans-bilayer movements

ATG9A			$ATG9A_{N99glyco}$		
Replicate 1	Replicate 2	Replicate 3	Replicate 1	Replicate 2	Replicate 3
702, 705, 709, 712, 713, 715,	702, 705, 715, 720, 725, 735,	702, 705, 733, 735, 737, 743,	708, 711, 712, 714, 718, 723,	708, 709, 711, 718, 722, 724,	708, 714, 730, 750, 753, 755,
718, 736, 747,	758, 766, 803,	757, 758, 771,	735, 745, 749,	725, 750, 752,	756, 733, 777,
750, 757, 758,	811, 818, 820,	780, 828,884,	750, 751, 753,	762, 764, 768,	780, 737, 803,
759, 785, 790,	821, 873, 933,	900, 944, 979,	754, 755, 789,	774, 776, 778,	812, 840, 883,
794, 796, 800,	954, 991, 994,	986, 991, 992,	790, 845, 851,	789, 793, 833,	918, 933, 935,
819, 890, 906,	996, 1003, 1013,	994, 996, 1003,	906, 931, 980,	902, 934, 958,	939, 971, 976,
921, 933, 940,	1020, 1091, 1170	1013, 1036, 1105,	991, 995, 996,	987, 991, 996,	991, 996, 1009,
955, 991, 994,		1124	1009, 1010, 1017,	1000, 1009, 1015,	1015, 1024, 1027,
1003, 1013, 1014,			1024, 1050, 1065,	1022, 1024, 1026,	1087, 1098, 1128,
1026, 1101, 1128,			1082, 1090, 1208,	1027, 1038, 1058,	1146, 1189, 1217
1229			1229	1194, 1236	
Tot. 34	Tot. 24	Tot. 25	Tot. 34	Tot. 35	Tot. 33

(b)

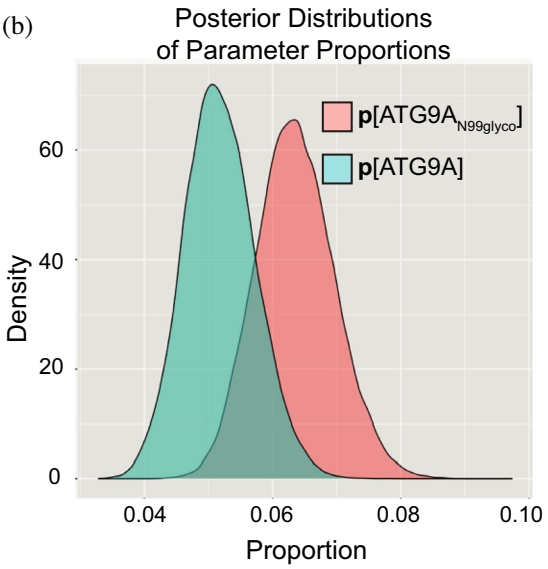

(c)

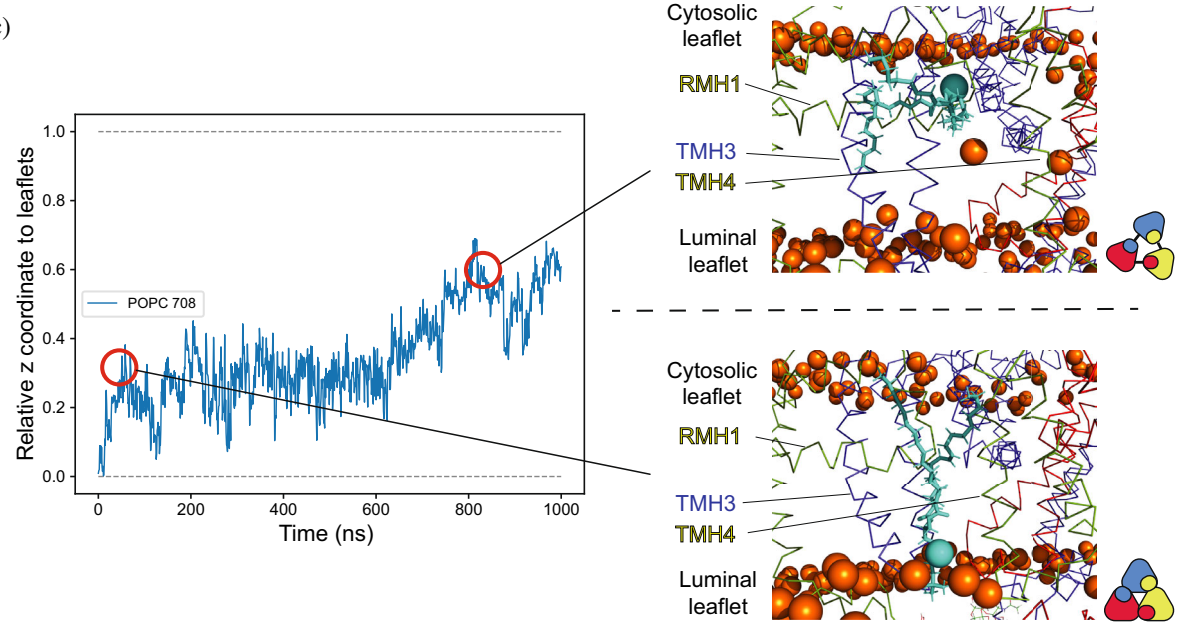

(d)

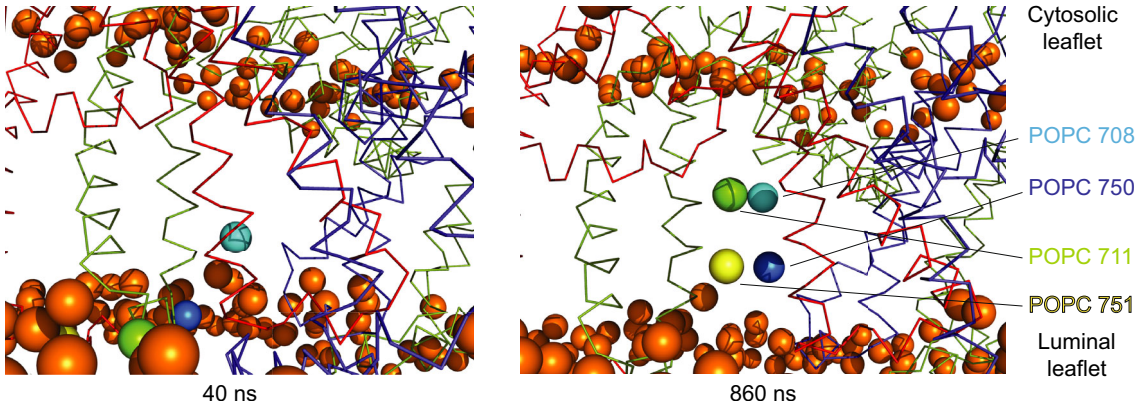

FIGURE 6 Legend on next page.

phases. In our case, steady-state measurements alone are insufficient, as they may not capture alterations induced by specific genetic modifications, such as ATG9A variants; thus it is necessary to normalize the measurements using specific ratios to accurately quantify autophagy flux (Klionsky et al., 2021).

To assess the effects of ATG9A *N*-glycosylation on autophagy flux, we generated two ATG9A variants, $ATG9A^{N99A}$ and $ATG9A^{N99D}$, which abolish the *N*-glycosylation sequon and thus impair *N*-glycosylation at the site. To assess the effects of ATG9A N-glycosylation on autophagy flux, we first investigated the potential pathogenicity of variants at the N99 and S101 sites, as both can impact the N-glycosylation sequon. We examined available data from gnomAD (Gudmundsson et al., 2022) and ClinVar (Landrum et al., 2020) and found no reported pathogenic or likely pathogenic variants at either site. In contrast, Alphamissense (Cheng et al., 2023) predicts several N99 variants (N99W, N99V, N99M, N99I, N99F, and N99C) as likely pathogenic, while no pathogenic or likely pathogenic variants were reported for S101. Based on these findings, we generated two ATG9A variants, $ATG9A^{N99A}$ and $ATG9A^{N99D}$, which abolish the *N*-glycosylation sequon and thus impair *N*-glycosylation at the site. To ensure that the endogenous ATG9A levels did not interfere with the analysis, we used both ATG9A knockout (KO) and control HEK293 cell lines (Figure S9). The ATG9A KO cell line provided a clean background where only the introduced ATG9A variants were expressed, allowing us to specifically evaluate their role in autophagy flux without the confounding effects of endogenous ATG9A. The autophagy flux was assessed by comparing LC3-II and SQSTM1 turnover in the presence and absence of bafilomycin A1, a lysosomal degradation inhibitor. This approach enabled us to determine whether the ATG9A variants enhance or impair autophagy by analyzing both markers' synthesis and degradation ratios. First, we validated the KO cell line by confirming that no levels of endogenous ATG9A were detected (Figure 7a), then, upon transient ATG9A variant overexpression, we measured the variants' effects on the autophagy marker synthesis and degradation ratios as compared to ATG9A WT (Figure 7). Based on our simulations, which suggested that N99 glycosylation may enhance lipid accessibility and cooperative conformational changes in ATG9A, we would have expected the N99 variants to show altered autophagic activity, potentially reflected in changes in LC3-II accumulation or in the turnover of the cargo adaptor SQSTM1/p62. However, our results did not show any statistically significant impact of the $ATG9A^{N99A}$ and $ATG9A^{N99D}$ variants compared to ATG9A WT (Figure 7a–c). This conclusion was based on the analysis of both LC3-II and SQSTM1/p62 levels, which showed no significant differences under the tested conditions.

2.6 | Autophagosome size analysis in ATG9A KO cells

In addition to flux assays, we evaluated a second experimental readout that is more directly related to membrane remodeling: autophagosome size. As the absence of ATG9A has been reported to cause an increase in LC3-positive vesicle size (Runwal et al., 2019), we investigated whether modifications at N99 produced comparable effects.

To this end, we quantified the average area of LC3-positive vesicles in ATG9A-KO HEK293/HEK293T cells reconstituted with either wild-type ATG9A or the N99 variants. KO cells transfected with empty vector (KO-Mock) exhibited enlarged vesicles compared to control cells (Ctl-Mock; $p = 0.0287$), consistent with a role of ATG9A in regulating autophagosome size. Re-expression of ATG9A WT restored vesicle size to

FIGURE 6 ATG9A N-glycosylation favors open states of the central cavity and facilitates partial trans-bilayer movements of phospholipids. (a) Analysis using LipidDyn of the POPC lipids showing partial trans-bilayer movements for each replica of ATG9A and $ATG9A_{N99glyco}$ ($n = 3000$ total frames per system sampled every 1000 ps). In $ATG9A_{N99glyco}$, we observed a higher average of phospholipids exhibiting partial trans-bilayer movements compared to ATG9A. (b) Bayesian analysis of lipid translocation frequencies in ATG9A (cyan) and $ATG9A_{N99glyco}$ (pink). Posterior distributions were obtained by modeling the number of lipid translocation events as binomial processes with unknown probabilities $p_{glyco}(ATG9A_{N99glyco})$ and $p_{non-glyco}(ATG9A)$, as described in the Methods. The density plots represent the posterior probability distributions of these parameters, showing that glycosylation is likely to increase the translocation probability ($P(p_{glyco} > p_{non-glyco}) = 0.93$). (c) Example of a lipid (POPC 708) inserting into the central cavity of ATG9A and undergoing reorientation and partial trans-bilayer movement in replicate1 of $ATG9A_{N99glyco}$. The left panel shows the time-wise relative position along the z axis of the head group of POPC 708 (blue line) with respect to the two leaflets. Here the value of 1 corresponds to the cytosolic leaflet and 0 corresponds to the luminal leaflet. The right panels show two representative frames at 30 ns (lower) and 860 ns (upper) of the simulation. The ATG9A structure is shown as a ribbon, highlighting its three protomers: A (red), B (blue), and C (yellow). Lipids headgroups are shown as orange spheres while POPC 708 is highlighted in cyan. The lipid headgroup is inserted in the central cavity at the domain-swapped interface CB (30 ns, lower) and then reorient horizontally while still maintaining the acyl tails in the favorable hydrophobic lipids' bilayer (860 ns, upper). Each panel includes a schematic representation showing the open and closed asymmetric conformations of ATG9A at the protomer interfaces. (d) Frame at 40 ns (left panel) and frame at 860 ns (right panel) extracted from replicate1 of $ATG9A_{N99glyco}$. The headgroups of some of the lipids undergoing partial trans-bilayer motions, POPC 708 (cyan), POPC 711 (green), POPC 750 (blue) and POPC 751 (yellow), are shown as spheres. We observed that multiple phospholipids inserted inside the central cavity.

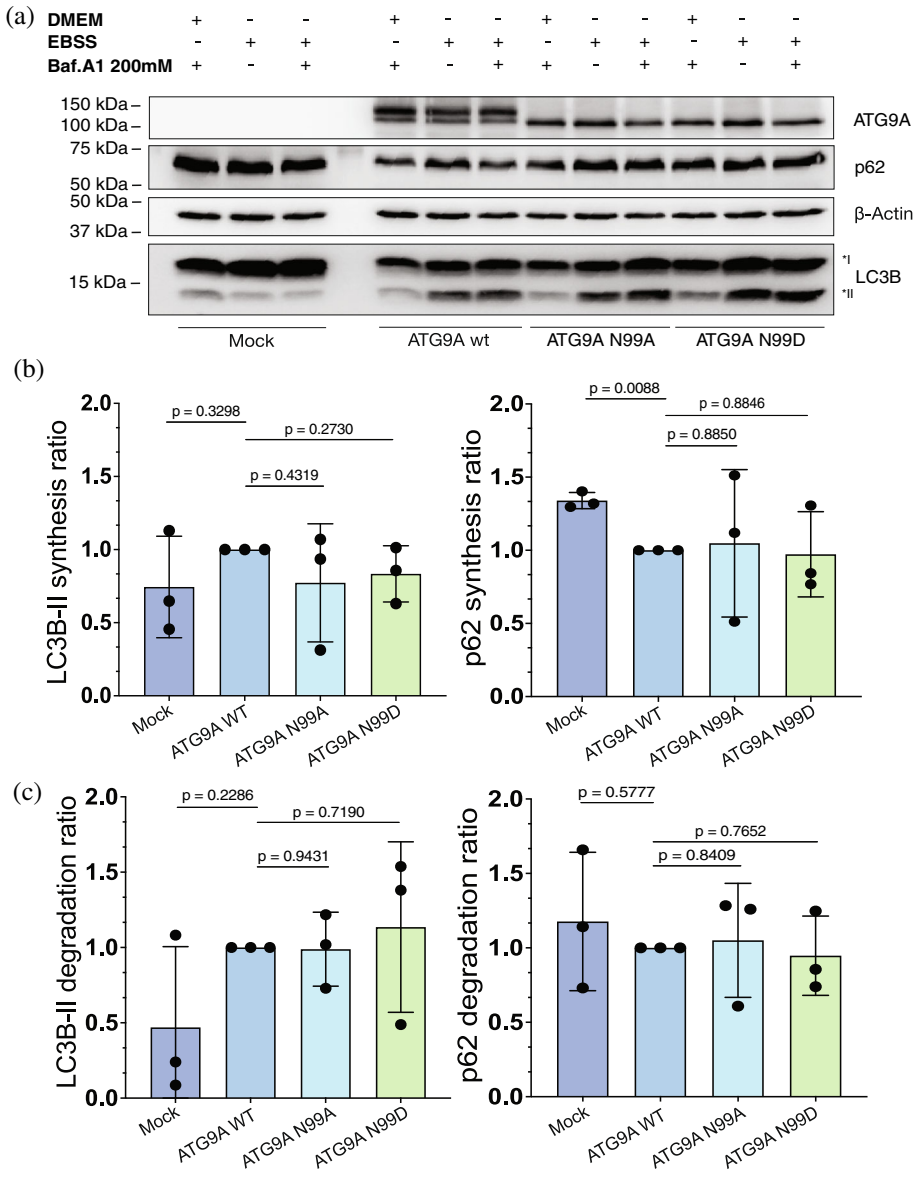

FIGURE 7 Abolishing *N*-glycosylation through mutagenesis is not sufficient to capture any difference in autophagosome synthesis and degradation in the ATG9A KO HEK293 cell line. (a) Western blot analysis of the LC3-II and p62 levels of ATG9A WT, ATG9A^{N99A} and ATG9A^{N99D} under starvation (EBSS medium) or rich-nutrient conditions (DMEM medium), in the presence of bafilomycin A1, a lysosomal degradation inhibitor, in the ATG9A KO HEK293 cell line. ATG9A^{N99A} and ATG9A^{N99D} samples were both loaded on a 15% gel along with ATG9A WT and the Mock condition (i.e., no overexpression). LC3-II and SQSTM1/p62 levels have been normalized with the housekeeping protein β-Actin levels in the same sample. (b) Analysis of the autophagosome formation rate (synthesis rate) following LC3-II (left) or SQSTM1/p62 (right) levels. The synthesis rate has been calculated as the rate of LC3-II (or SQSTM1/p62) levels in the presence of the inducer (i.e., EBSS) and the inhibitor (i.e., Bafilomycin A1) divided by the LC3-II (or SQSTM1/p62) level in the presence of the inhibitor alone. (c) Analysis of the autophagosome degradation rate following LC3-II (left) or SQSTM1/p62 (right) levels. The degradation rate has been calculated as the rate of LC3-II (or SQSTM1/p62) levels in the presence of the inducer (i.e., EBSS) and the inhibitor (i.e., Bafilomycin A1) divided by the LC3-II (or SQSTM1/p62) level in the presence of the inducer alone. Data are shown as mean ± SD; individual data points represent biological replicates ($n = 3$). Statistical analysis was performed using Welch's unequal variances *t*-test.

control levels, whereas expression of the ATG9A^{N99A} and ATG9A^{N99D} variants failed to rescue the phenotype, resulting in significantly larger vesicles than in KO-WT cells ($p = 0.0117$ and $p = 0.0148$, respectively) (Figure 8).

When combined with the autophagy flux assays, which showed no significant differences between WT and N99 variants in LC3-II and SQSTM1/p62 turnover, these results suggest that N-glycosylation at N99 might not be essential for the overall autophagic process but may act as a fine-tuning regulator. Specifically, our data support a model in which N99 and its glycosylation state contribute to shaping autophagosome morphology by modulating the conformational dynamics and lipid transport properties of ATG9A, without altering bulk flux through the autophagy pathway.

3 | DISCUSSION

In this study, we combined computational and experimental approaches. In the first part of the work, we focused on microsecond MD simulations to explore the mechanistic effects of N99 glycosylation on ATG9A dynamics and lipid scrambling, while the final sections evaluated experimental readouts (autophagy flux and autophagosome size) to assess whether these predictions translate into cellular phenotypes. The ATG9A hydrophilic central cavity supports phospholipid headgroup insertion, reorientation, and partial transbilayer movements, consistent with lipid scrambling activity observed in experimental assays. Of note, the MD simulations presented here focused on the fully N99-glycosylated form of ATG9A, using a complex-type *N*-glycan commonly found in human proteins. However,

in vivo, ATG9A trimers are likely to consist of monomers with heterogeneous glycosylation states due to variable glycan processing or occupancy at N99. This potential asymmetry within a trimeric assembly could influence both the local conformational dynamics and the functional behavior of the protein, such as membrane remodeling capacity or interaction with autophagy regulators. Since the loop containing N99 and its attached glycans remains unresolved in the current cryo-EM structures, and experimental characterization of this region is complicated by glycosylation heterogeneity, our simulations provide a valuable framework for exploring the structural and functional consequences of N-glycosylation on ATG9A. Future work incorporating mixed glycoforms or partial glycosylation states may further refine our understanding of how this post-translational modification modulates ATG9A activity.

Intrinsic flexibility is a conserved feature of ATG9 proteins, as both ATG9A and ATG9B exhibit significant conformational plasticity, suggesting this is an inherent characteristic crucial for their function. A key determinant of this flexibility is the HINGE region, defined in *S. pombe* Atg9 (SpAtg9) as the cytoplasmic helices CH6–CH10 (Matoba et al., 2020), whose structural differences between cryo-EM structures and AlphaFold models further emphasize its role in modulating ATG9A dynamics and lipid interactions (Chiduza et al., 2024). Our findings support the idea that this region directly impacts lipid handling and transport, aligning with its proposed role in autophagy. Glycosylation may fine-tune this inherent flexibility, rather than being strictly required for lipid scrambling activity. Chiduza et al. demonstrated that human ATG9B, which contains a conserved N-glycosylation motif, functions as a lipid scramblase (Chiduza et al., 2024). While they suggested that ATG9B may be glycosylated based on the presence of this motif, they did not experimentally verify its glycosylation status or assess scrambling activity in its absence. In contrast, our study shows that glycosylation might modulate ATG9A dynamics. Our results suggest that *N*-glycosylation strengthens cooperative interactions between protomer conformations, facilitating lipid insertion and partial translocation within the central cavity. This aligns with the proposed mechanism of ATG9A's role in autophagy, where it aids lipid redistribution across the phagophore membrane to support elongation and autophagosome biogenesis. Our findings, however, suggest that abolishing N-glycosylation through mutagenesis does not result in a detectable alteration of autophagic activity in bulk flux

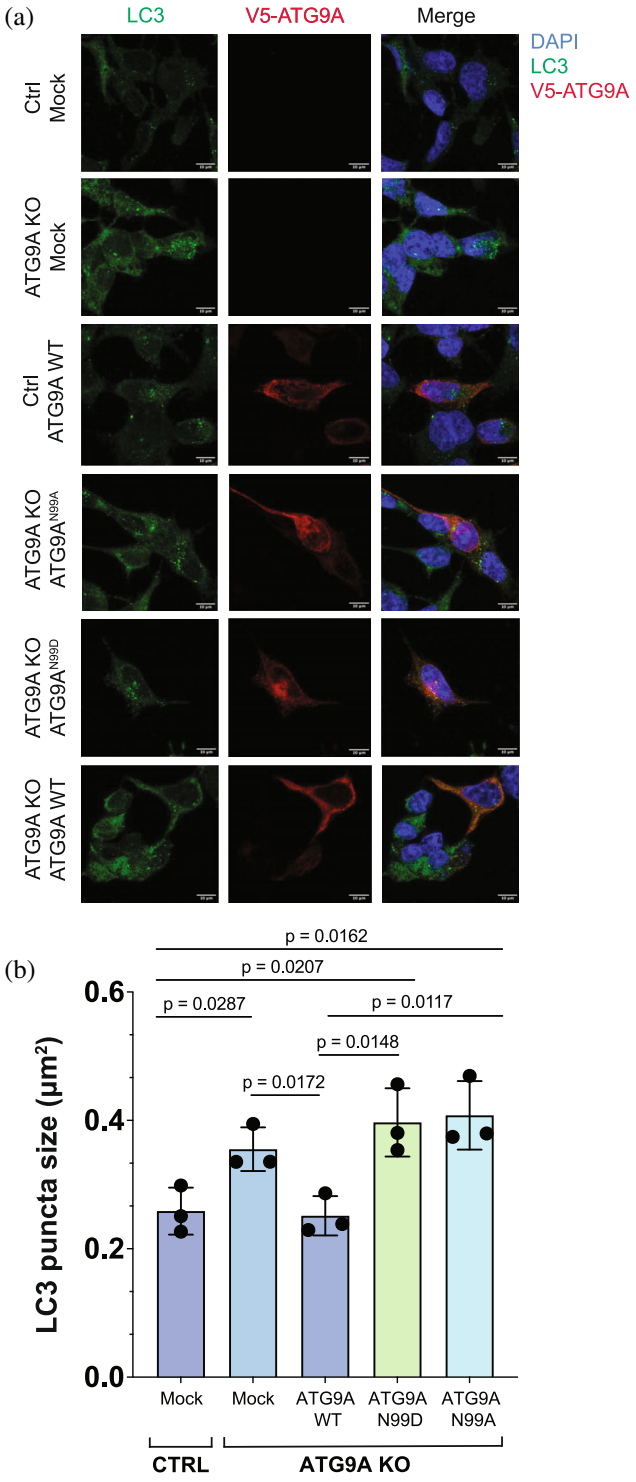

FIGURE 8 Analysis of autophagosome vesicle size in ATG9A KO and control HEK293 cells. (a) Representative confocal immunofluorescence images of control (Ctl-Mock) and ATG9A knockout (KO) HEK293 cells transfected with empty vector (KO-Mock), V5-tagged wild-type ATG9A (WT), or the V5-tagged ATG9A^{N99A} and ATG9A^{N99D} variants. Nuclei were stained with Hoechst (blue), LC3B with anti-LC3B antibody (green), and ATG9A with anti-V5 antibody (red). Scale bars, 10 μm. (b) Quantification of LC3-positive vesicle area. Vesicle size was first averaged per cell, and these values were then averaged across the analyzed cells for each condition. Approximately 30 cells were analyzed per condition in each replicate. Data are shown as mean ± SD; individual data points represent biological replicates ($n = 3$). Statistical analysis was performed using an unpaired *t*-test.

assays, such as LC3B-II and p62 turnover. While this negative result may initially appear inconclusive, it is in fact informative: it suggests that glycosylation at this site is not essential for maintaining global autophagic throughput under the tested conditions. However, this does not preclude the possibility that glycosylation influences more specific or localized aspects of ATG9A function, such as autophagosome maturation, membrane curvature modulation, vesicle size, or cargo selectivity. Bulk flux assays are inherently limited in their sensitivity to such molecular-level phenomena, particularly when compensatory mechanisms may buffer functional deficits. As such, the lack of flux alteration should be viewed as a meaningful outcome that helps refine the mechanistic hypotheses. In addition to the autophagy flux assays, our analysis of LC3-positive vesicle areas provided further insight into the cellular effects of N99 glycosylation. Re-expression of wild-type ATG9A in ATG9A-KO cells restored vesicle size to control levels, whereas the N99A and N99D variants failed to rescue the enlarged-vesicle phenotype. These findings indicate that, although N-glycosylation at N99 is not required for maintaining overall autophagic flux, it contributes to the regulation of autophagosome morphology. This observation aligns with our MD simulations, which predicted that glycosylation enhances cooperative protomer dynamics and increases lipid accessibility of the central cavity, potentially promoting membrane remodeling and vesicle curvature regulation. Together, these results suggest that glycosylation fine-tunes ATG9A-mediated membrane transformations that influence autophagosome size, rather than acting as an essential determinant of autophagic bulk flux.

More broadly, glycosylation is known to serve diverse modulatory roles across many classes of membrane proteins (Reily et al., 2019; Varki, 2017), and our findings suggest that ATG9A may similarly use N99 glycosylation to fine-tune local conformational dynamics and functional outcomes. Beyond its potential role in modulating lipid scrambling, our findings and previous studies suggest that N-glycosylation at N99 may influence additional aspects of ATG9A function. The N99-containing luminal loop is positioned close to structural elements that shape the central cavity and contribute to membrane remodeling, raising the possibility that glycosylation helps stabilize conformations favorable for curvature sensing or modulation. Moreover, the enhanced cooperativity between protomers that we observed in the glycosylated form could fine-tune the exposure of specific interfacial regions, thereby influencing protein–protein interactions beyond ATG2A, such as with other autophagy regulators or scaffolding factors. In this way, glycosylation may serve as a context-dependent modulator of ATG9A activity, affecting autophagosome morphology or local membrane dynamics without altering bulk autophagy flux. To uncover subtler roles of glycosylation, future studies involving in vitro lipid scramblase assays, membrane reconstitution systems, or structural analyses will be instrumental in dissecting how glycosylation may affect ATG9A's dynamic behavior and interactions within the autophagy machinery. However, it is important to recognize that in vitro lipid scramblase assays, while powerful, may not fully recapitulate the complexity of the cellular environment. As discussed in Chiduza et al., such assays can lack sensitivity to subtle changes in scramblase activity and may not capture modulation by membrane curvature, protein partners, or local lipid composition. Despite these limitations, we anticipate that glycosylation may subtly enhance lipid insertion and headgroup translocation within the ATG9A cavity, as observed in our simulations. Therefore, we hypothesize that future reconstitution experiments could reveal increased scrambling kinetics or altered lipid specificity in the glycosylated form of ATG9A, particularly under membrane conditions that mimic early autophagic membranes. Beyond the central cavity, our simulations also revealed dynamic openings of the lateral and perpendicular cavities at the protomer interfaces. These side cavities, which have been proposed as lipid entry or exit routes and potential handoff sites for ATG2A, became more accessible in glycosylated ATG9A, particularly in clusters enriched in open conformations. This observation suggests that glycosylation may not only fine-tune the conformational dynamics of the central pore but also indirectly regulate lipid access through auxiliary cavities, thereby contributing to ATG9A's role in lipid redistribution during autophagosome biogenesis. The analysis of glycan–protein contacts revealed that the N99-linked glycan engages in reproducible yet transient interactions with residues located in the luminal loops adjacent to the glycosylation site. While the specific contacts varied between protomers, several residues consistently appeared in contact with the glycan in more than 20% of the trajectory frames (Figure S7). These findings suggest that the glycan may transiently stabilize local conformations of the luminal region, thereby influencing the gating of the central cavity or interactions with neighboring protomers. Future mutagenesis of these residues could help determine whether such glycan-mediated contacts contribute directly to ATG9A's conformational dynamics and regulatory role in autophagy. These assays, especially when performed alongside structural or single-molecule readouts, could provide key validation for the regulatory role of glycosylation. Furthermore, variations in ATG9A functionality, potentially influenced by post-translational modifications like glycosylation, could impact autophagosome size or morphology. This highlights the need for targeted experiments to explore this relationship. On the other hand, we observed partial phospholipid traversal at protomer interfaces, suggesting that complete transbilayer movements may require

enhanced sampling techniques or larger membrane models to incorporate the effects of curvature and biophysical membrane properties. The lipid environment surrounding ATG9A is likely to be a key modulator of its function. As ATG9A localizes to compartments with distinct lipid compositions, such as the trans-Golgi network, endosomes, and phagophore membranes, the biophysical properties of these membranes, including lipid packing, thickness, and curvature stress, could influence its conformational dynamics and scramblase activity. For instance, local variations in cholesterol, phosphatidylethanolamine, or phosphatidylinositol phosphates may impact how ATG9A engages with and translocates lipids. While our current simulations used a standard POPC:CHL1 bilayer, future studies using alternative membrane compositions or coarse-grained simulations could provide valuable insight into how lipid heterogeneity contributes to ATG9A regulation in different cellular contexts. Comparisons with other phospholipid scramblases suggest that regulatory mechanisms often rely on conformational flexibility and context-dependent modulation. For instance, TMEM16 scramblases are activated by calcium binding, which induces structural rearrangements that open lipid transport pathways, while XKR proteins become active upon caspase cleavage (Kodigepalli et al., 2015). Although ATG9A does not share these activation mechanisms, our results suggest that glycosylation and conformational asymmetry may play analogous modulatory roles. In particular, the dynamic interprotomer asymmetry observed in our simulations may reflect a broader regulatory principle shared with other scramblases, where structural heterogeneity fine-tunes lipid transport activity and enables context-specific interactions with other proteins. Finally, our simulations show that ATG9A can adopt asymmetric conformations at protomer interfaces, in contrast with symmetric configurations observed in cryo-EM structures. This conclusion is supported by multiple independent metrics, including interface contact scores, clustering analyses, and per-protomer RMSD relative to cryo-EM references, all of which consistently point to asynchronous protomer transitions. The emergence of asymmetric protomer conformations in our simulations also raises the intriguing possibility that such dynamic features contribute to the functional interaction of ATG9A with binding partners such as ATG2A. Structural studies have proposed that ATG2A binds asymmetrically to the ATG9A trimer (van Vliet et al., 2022), and the observed conformational heterogeneity could facilitate or regulate this interaction by presenting a preferential binding interface. This supports a model in which ATG9A asymmetry is not only tolerated but may be functionally exploited to modulate complex assembly and lipid transfer activity during autophagy. While the asymmetric protomer conformations observed in our simulations offer novel insights into ATG9A dynamics, we acknowledge the importance of carefully considering potential biases introduced by molecular dynamics itself. Asymmetry can, in principle, arise from limitations in simulation timescales, force field accuracy, or starting model configurations. However, the reproducibility of this asymmetry across independent replicas, its localization to flexible regions such as the N99-containing loop, and the absence of unphysical structural distortions support the interpretation that these deviations reflect genuine dynamic behavior rather than simulation artifacts. Nonetheless, future studies using alternative force fields, longer trajectories, and enhanced sampling methods will be valuable to fully validate the robustness of this asymmetry and its potential physiological relevance. Future cryo-EM studies aiming to resolve this heterogeneity could benefit from approaches that preserve asymmetry, such as classification and refinement without symmetry enforcement or symmetry expansion followed by focused classification and refinement using signal subtraction. Furthermore, future technological improvements leading to better signal-to-noise ratios, as well as advances in time-resolved cryo-EM, which allow the characterization of dynamic intermediates and transient conformations, may help uncover functionally relevant asymmetric states of ATG9A (Mäeots & Enchev, 2022). Integrating such approaches with biochemical reconstitution of ATG9A in lipid nanodiscs or vesicles under various functional conditions may further aid in capturing asymmetric or partially open conformations that reflect its physiological dynamics. Our work emphasizes the importance of incorporating glycosylation in computational studies of ATG9A dynamics and lipid scrambling. The methods developed here can be extended to study other scramblases and flippases, advancing our understanding of lipid transport mechanisms in various cellular contexts.

4 | MATERIALS AND METHODS

4.1 | Preparation of the starting structure

We used as starting structures for the MD simulations the cryo-EM structures of human ATG9A homotrimer in the closed state (PDB entry 7JLP chain A, B, and C, (Maeda et al., 2020)) selecting residues 36–522 for our construct. This structure was chosen because it is the only cryo-EM model of ATG9A so far obtained in nanodiscs (3.4 Å resolution), using a native-like lipid composition of 1-palmitoyl-2-oleoyl-sn-glycero-3-phosphocholine (POPC): 1-palmitoyl-2-oleoyl-sn-glycero-3-phosphatidylserine (POPS) at a 3:1 ratio. Although 7JLP includes residues up to 532, we limited the construct to residue 522 to ensure consistency with other high-resolution ATG9A structures, including those in the open conformation (e.g., 7JLQ and 6WR4), which also resolve only up to residue 522. Other cryo-EM structures, such as 6WQZ, include additional C-terminal residues

(up to 587), including residues 523–532. However, these segments are not consistently resolved across available structures and exhibit increased conformational variability. AlphaFold predictions (AF-Q7Z3C6-F1) also suggest the presence of C-terminal helical elements (residues 636–656 and 695–723) potentially interacting with the folded core, as supported by cross-linking data (van Vliet et al., 2022). As these regions are not resolved in any current experimental structures, they were excluded from our model to avoid incorporating speculative or poorly defined structural elements. We removed the lipid molecules that were present in the cryo-EM structures. We used MODELER v. 9.15 (Eswar et al., 2007) to reconstruct the missing coordinates in the region 96–108, keeping the rest of the coordinates in the original positions. We generated 100 different models with MODELER for ATG9A. We then used the statistically optimized atomic potential protein orientation-dependent score (SOAP-Protein-OD, (Dong et al., 2013)) to evaluate the quality of the models and to rank them. SOAP-Protein-OD is an orientation-dependent potential. It is optimized for scoring protein models by evaluating the environment of residues in the models with respect to the expected environment from experimental structures. We used SOAP potential since it was developed to assess protein–protein interfaces and multiple-chain systems (Dong et al., 2013). We also calculated the normalized DOPE z score and checked that the models do not have scores with positive values, which indicates low-quality models. We selected the top five models ranked on the SOAP-Protein-OD score, and we analyzed them by calculating Van der Waals clashes using Arpeggio (Jubb et al., 2017) and by visual inspection of the reconstructed regions. Between these five models, we selected one model for ATG9A in which the reconstructed regions have similar orientations between the protomers and do not make extensive contact with the rest of the protein to avoid a bias in the initial conformation for MD simulations. We used the selected model of ATG9A to design a glycosylated form of ATG9A ($ATG9A_{N99glyco}$). ATG9A is glycosylated with a complex-type *N*-glycan at N99 (Young et al., 2006), located in a loop facing the luminal side of the membrane. We modeled the *N*-glycosylation of each protomer of $ATG9A_{N99glyco}$ with a common complex-type structure of *N*-glycans in humans (Fadda, 2022) using the tools available in CHARMM-GUI version 3.8 (Lee et al., 2019). *N*-glycans at N99 are complex, biantennary, mono sialylated and core fucosylated (GlyTouCanID G65761WK). This type of *N*-glycosylation is compatible with the localization of the protein in the trans Golgi.

4.2 | Design of ATG9A and $ATG9A_{N99glyco}$ systems with lipid bilayers

We used the selected model of ATG9A and $ATG9A_{N99glyco}$ to build the systems with lipid bilayers. We generated the systems by CHARMM-GUI version 3.6 (Jo et al., 2008; Lee et al., 2016, 2019). In CHARMM-GUI, we solvated the cavities of ATG9A. We used PyMOL to include in our systems only the water molecules inside the cavities using a cutoff of 4.5 Å for the distance between the water molecules and protein atoms lining the cavities. We identified the protein atoms lining the cavities of ATG9A by using CAVER 3.02 software (Chovancova et al., 2012). We used as an initial starting point for the cavity calculations the so-called "center of gravity" (Chovancova et al., 2012) defined by V440 of protomers A, B, and C. This residue is located on the top of the structure on the cytosolic side and oriented towards the central cavity of ATG9A. We used as parameters for the CAVER calculations a probe radius of 1.2 Å, comparable to the size of a water molecule (Manak et al., 2017), a shell radius of 15 Å, a shell depth of 4 Å, and a clustering threshold of 8 Å. We included 307 water molecules inside the cavities of ATG9A. We included the same number of water molecules inside the cavities of $ATG9A_{N99glyco}$.

We defined the protonation of the histidines by visual inspection of the experimental structures and by the predictions of PROPKA 3 (Olsson et al., 2011) and H++ webserver (Anandakrishnan et al., 2012). We defined all the histidines as ε tautomer apart from H161 as δ tautomer. We capped the N- and C-terminus with the acetyl (ACE) and *N*-methylamide (CT3) groups. We inserted the protein inside a lipid bilayer with the size of 160, and 160 Å in the x and y dimensions, respectively, and composed of 1-palmitoyl-2-oleoyl-sn-glycerol-3-phosphocholine (POPC) 75% and cholesterol 25%. We here used a standard lipid composition for the bilayer since the detailed compositions of phagophore and autophagic membranes remain poorly understood due to challenges in isolating and characterizing these transient and dynamic structures (Li et al., 2021; Schmitt et al., 2022). The lipid bilayer was symmetric and included 720 lipids. To orient the protein in the membrane, we used the Orientation of Proteins in Membranes (OPM) webserver (https://opm.phar.umich.edu/ppm_server, Lomize et al., 2012) in CHARMM-GUI. The OPM database uses the Positioning of Proteins in Membrane approach to determine the orientation of the protein in a membrane bilayer by minimizing its transfer energy with respect to several geometric variables in a coordinate system whose z axis coincides with the membrane bilayer normal. The systems were solvated in a rectangular box of water molecules with a minimum distance of 20 Å between the protein atoms and the edge of the water layers, including around 100 water molecules per lipid. We used a solvent model TIP3P adjusted for CHARMM force fields with Lennard-Jones sites on the hydrogen atoms (MacKerell et al., 1998).

4.3 | Molecular dynamics simulations

We equilibrated the systems according to the CHARMM GUI procedure that involves minimization followed by steps in which positional restraints for lipid head groups and protein backbone atoms are gradually removed. We carried out three replicates of 1-μs all-atom explicit solvent MD simulations for ATG9A and ATG9A$_{N99glyco}$ with the CHARMM36m force field (Huang et al., 2017; Klauda et al., 2010) (Table 1). We performed the MD simulations with GROMACS (Abraham et al., 2015). We initialized each replicate using different atomic velocities. We carried out the simulations at a concentration of 0.15 M of NaCl, neutralizing the net charge of the system. We simulated each system under periodic boundary conditions. We used the LINCS algorithm to constrain the hydrogen bonds (Hess et al., 1997) and applied a time step of 2 fs. We applied the particle-mesh Ewald (PME) summation scheme (Petersen, 1995) to calculate long-range electrostatic interactions using a Fourier spacing of 1.2 Å and interpolation order of 4. Van der Waals and Coulomb interactions were truncated at 12 Å. We performed productive MD simulations in the NPT ensemble at 310 K and 1 atm. We used a Nose-Hoover thermostat (Nosé, 1984) for temperature control, with coupling every 1 ps, and a Parrinello-Rahman barostat (Parrinello & Rahman, 1981) for pressure control, with coupling every 5 ps. We used semi-isotropic coupling in which the lateral pressure Pxy and normal pressure Pz dimensions are coupled independently. Other details are provided in the input files in OSF (https://osf.io/c4aqu/).

We joined the three individual 1-μs replicates of ATG9A and ATG9A$_{N99glyco}$ to obtain two 3-μs ensembles of conformational states (i.e., concatenated trajectories, $n = 3000$ frames, 1000 ps timestep) that were used in the analysis. To assess convergence and reproducibility, we monitored the temporal evolution of Cα RMSD and radius of gyration. In all cases, RMSD values plateaued within the first ∼200 ns, with stable fluctuations thereafter. Replicates sampled consistent conformational states, as verified by clustering analyses and contact score distributions, indicating reproducible dynamics across independent trajectories. Importantly, the asymmetric conformations reported here were observed in multiple replicates and were not restricted to a single trajectory, supporting their robustness rather than being artifacts of simulation initialization or limited timescales. We calculated the minimum distance between the protein atoms and its periodic images to find potential periodic boundary artifacts. In all the simulations, we observed a minimal distance always higher than 28 Å.

4.4 | Analysis of conformational changes and protein flexibility

We calculated the RMSD values of all the Cα atoms with respect to the cryo-EM structures of the closed (PDB ID: 7JLP) (Maeda et al., 2020) and open state (PDB ID: 6WQZ) (Guardia et al., 2020). We excluded from the analysis the flexible loop (residues 96–111) that we reconstructed by MODELER in the starting models. To better visualize the open/closed conformations that could potentially be sampled independently by each protomer, we then calculated (i) RMSD of all Cα atoms of every single protomer (i.e., chain A, B, C) and (ii) RMSD of the Cα atoms of only the swapped transmembrane helices of each protomer (named TMH3 and TMH4) (Maeda et al., 2020) with respect to the experimental cryo-EM structures of the closed and open state. In both cases, we used all the helical transmembrane regions of the protomers for the rigid body superposition (residues 43–55, 59–86, 119–127, 130–168, 180–193, 206–225, 245–256, 279–322 and 472–507 of each protomer). In addition, we calculated the RMSD of TMH3–4 for each protomer relative to the closed cryo-EM structure across the 3-μs trajectories, with both the fitting and the RMSD calculation performed on the same TMH3–4 segments. This analysis allowed us to account for the possible movement of the entire protomer relative to the trimer, rather than only local rearrangements of TMH3–4.

We calculated a contact score based on the analysis of the fraction of contacts present only in the experimental cryo-EM structure of the closed state when compared to the open one. We employed the software CONtact Analysis (CONAN) (Mercadante et al., 2018) to analyze intramolecular contacts in the cryo-EM structures of the closed (PDB ID: 7JLP) and open state (PDB ID: 6WQZ) of ATG9A. We used a cutoff r_{cut} value of 10 Å, r_{inter} and $r_{high\text{-}inter}$ values of 5 Å, using a protocol previously employed (Degn et al., 2022). We processed the data to obtain a list of contacts identified only in the closed structure. We then filtered these contacts, including only the ones formed by residues in the regions of ATG9A involved in the conformational changes. Thus, we included contacts between residues 367–431 of the exchanged (i.e., domain-swapped) transmembrane helices TMH3-4 of each protomer and region 316–335 of the same protomer, and region 389–426 of the corresponding swapping protomer. The domain-swapping order of protomers is (i) protomer A with protomer C, (ii) protomer B with protomer A, and (iii) protomer C with protomer B. We then monitored the presence of these contacts during the MD trajectory and calculated a timewise contact score as the fraction of contacts, that is, values close to 1 mean that nearly all the contacts are present and the structure is similar to the closed one, while a value close to 0 means that nearly all the contacts are absent. We calculated the per-residue Cα-atoms Root Mean Square Fluctuations (RMSF) as the flexibility index. We calculated RMSF as averaged over consecutive and non-overlapping time windows of 10 and 100 ns along the trajectories, as used for other proteins (Di Rita et al., 2018; Lambrughi et al., 2020). The analysis of the glycans, protein and

lipid atoms in the surround of the N-glycans has been performed using a 6 Å distance cutoff.

4.5 | Analysis of conformational states and clustering

We further analyzed the results of the contact score to perform clustering of the trajectory frames. The distance between frames was determined by the Euclidean distance using the contact score values of each domain-swapped protomer interface as coordinates. To consider the threefold symmetry of the ATG9A homotrimer, we performed the clustering using the minimum of the distances to each of the three possible rotations of the protein for each pair of frames (e.g., a structure with one open interface AC and two closed interfaces BA and CB is considered equivalent to a structure with one open interface BA and two closed interfaces CB and AC). We implemented a script (see OSF, https://osf.io/c4aqu/) to perform quality-threshold clustering (Heyer et al., 1999) with a threshold of 0.45, discarding clusters with fewer than 60 frames (<2% of the total). For each cluster, we determined its occurrence in the combined trajectories and its representative structure as the trajectory frame of the cluster with the minimum mean square distance to the rest of the frames in the cluster. To estimate the similarity between the sets of AC/BA/CB contact scores defined by each cluster in ATG9A and $ATG9A_{N99glyco}$, we calculated as measurements the (i) Jaccard similarity and (ii) weighted Jaccard similarity to also consider the frequencies of the values. The results are in both cases a value between 0 and 100%, where 100% indicates identical sets, and 0 indicates no similarity. To further stratify these sets, we calculated their associated kernel density distribution of the RMSD values of the Cα atoms of the swapped transmembrane helices TMH3-4 of each with respect to the experimental cryo-EM structures of the closed and open state.

4.6 | Independence analysis of the closed/open status of protomers

We used an in-house Python tool to evaluate the dependence/independence relationship of the open/closed status of each individual protomer of ATG9A (A, B, and C) with respect to the open/closed status of the other protomers (https://osf.io/c4aqu/). This allowed us to shed light on potential ongoing cooperativity in the conformational changes of the protomers. As input data for the analysis, we used the contact score values calculated for each protomer on the combined 3-μs trajectories of ATG9A and $ATG9A_{N99glyco}$ ($n = 3000$ frames, 1000 ps timestep). We applied a cutoff of 0.5 to classify the states as open or closed based on the distribution of contact score data, as this value appeared to effectively distinguish between them. As statistical models, we utilized Log-Linear Models (LLMs) with the Poisson family to fit the data and calculate deviance and log likelihood. These models are suitable for capturing the complex interactions and dependencies within the system and model the relationship between categorical variables (open/closed status of proteins) that have binary outcomes (open or closed) while considering potential nonlinear dependencies. The models investigated include complete independence, joint independence, conditional independence, and a homogeneous association model, each focusing on different combinations of relationships between the protomer open-closed status. We used chi-squared statistics to assess the difference in the deviance between different models and assess their goodness-of-fit and determine whether they are significantly different from each other. Furthermore, we employed Tukey Honestly Significant Difference (HSD) tests to analyze the deviance and log likelihood data, providing insights into the statistical significance of the model comparisons.

4.7 | Analysis of protein tunnels and channels

We used the standalone version of CAVER 3.02 software (Chovancova et al., 2012; Manak et al., 2017) to monitor the cavities of ATG9A and how they evolve during the MD trajectories.

Due to the complex branched network of tunnels in ATG9A, we selected different starting points as a reference for searching cavities using CAVER. In detail, we selected: (i) the centroid defined by considering all the atoms of K363 and K359 of all protomers (i.e., chain A, B, C) to monitor the central cavity, (ii) the centroid defined by considering all the atoms of E323, A329, Y358 of a protomer and R422 of the corresponding swapped protomer (i.e., for chain A, we selected E323, A329, Y358 of chain A and R422 of chain C) to monitor each of the three lateral cavities, (iii) the centroid defined by considering all the atoms of Y316, L354 of a protomer and F382 of the corresponding swapped protomer (i.e., for chain A, we selected Y316, L354 of chain A and F382 of chain C) to monitor each of the three perpendicular cavities. We selected these residues by visual inspection of the structures in PyMOL. We performed the cavity calculations on 20 structures extracted from each concatenated 3-μs trajectory ($n = 3000$ frames, 1000 ps timestep) and each structural state identified from the clustering of the contact score. We selected the 20 structures with the lowest mean squared pairwise distance to other frames in the cluster. As a reference for comparing calculated tunnels, we included calculations on the starting models of the open and closed states.

We monitored the cavities with probe radii of 1.2 Å designed to resemble the size of a water molecule. As CAVER parameters, we used a shell radius of 13 Å, a shell depth of 4 Å, and a clustering threshold of 12 Å. We clustered the cavities using the hierarchical average-link clustering method of CAVER by which two cavities are clustered based on the dissimilarity of their pathways in the protein, calculated by dividing each tunnel in a sequence of *N* consecutive points starting from the reference site and then calculating their pairwise distance. We used in-house Python and R scripts to (i) follow the evolution of the cavities during the MD trajectories, calculate the average radius and length of tunnels, and identify the residues lining the cavities. We used PyMOL to plot the cavities and graphically visualize them. Here, we focused on comparing the top 10 clusters of tunnels identified by CAVER, ranked based on the quantification of their tunnel throughputs.

4.8 | Analysis of membrane properties and protein-lipid contacts

We used *LipidDyn* (Scrima et al., 2022) to calculate the lipid bilayer properties and dynamics and protein-lipid contacts. During the simulation, we monitored the lipid transbilayer (i.e., scrambling) movements. The implementation of the lipid transbilayer module was officially included in the *LipidDyn* GitHub repository on 14/07/2023 (https://github.com/ELAB/LipidDyn/pull/157). *LipidDyn* uses the *LeafletFinder* class of MDAnalysis (Michaud-Agrawal et al., 2011) to identify the leaflet of the bilayer and the lipids belonging to them, considering atoms in their headgroups as representative atoms of each molecule. *LipidDyn* employs a reimplementation of *FATSLiM* software to estimate the bilayer thickness as the distance vector between neighborhood-averaged coordinates of each lipid and its neighbors in the opposite leaflet, using a cut-off distance of 60 Å. Furthermore, the calculation of APL is performed by a neighbor search of each lipid and computation of a Voronoi tessellation. As a note, we did not discuss in this study the analyses of membrane curvature since we could not estimate relevant differences among ATG9A and ATG9A$_{N99glyco}$ and larger bilayers would be required. *LipidDyn* incorporates an analysis module to track and analyze the lipid transbilayer movements. This tool uses the positions of the leaflet groups calculated from the *LeafletFinder* class to estimate the shape of the surface of the two leaflets to provide a reference for calculating the lipid transbilayer movements. The surface estimation is performed through a linear regression model, using four parameters as the polynomial degree of the equation. The tool then tracks the positions of lipid headgroups, enabling the identification of lipids that undergo transbilayer movements by using distance cutoffs from the two leaflets. We considered lipids that undergo even partial trans-bilayer movements using as a distance cut off 20% of the distance between the two leaflets of the bilayer. Furthermore, it calculates the contacts of the identified lipids with proteins using a distance cut-off of 6 Å. Additionally, we computed glycan–protein contacts across all MD trajectory frames. A contact was defined as the presence of any glycan and protein heavy-atom pair within 4 Å. For each residue, we calculated the frequency of contact as the percentage of frames in which it was in contact with the glycan. Only residues with contact frequencies above 20% were reported.

4.9 | Bayesian analysis of lipid translocation events

To evaluate whether N-glycosylation at N99 affects the probability of POPC lipid translocation, we used a Bayesian binomial model implemented in Stan (Stan Development Team, 2025; version 2.32.2) via the CmdStanR interface (Gabry et al., 2025; version 0.9.0.9000) in R (R Core Team, 2025; version 4.5.1) using RStudio (Posit Team, 2025; version 2025.09.1 + 401). For each condition (glycosylated and non-glycosylated ATG9A), the number of lipids undergoing trans-bilayer movement in each of three replicate simulations was modeled as a binomial process with unknown probabilities p_{glyco} and $p_{non-glyco}$. The total number of POPC lipids in the system ($n = 540$) was used as the number of trials in each binomial likelihood. Independent Beta(1, 1) priors were assigned to both probability parameters. Posterior distributions were obtained by Markov chain Monte Carlo sampling (four chains, 10,000 warm-up and 10,000 sampling iterations per chain), and convergence was confirmed by R-hat <1.01 and visual inspection of trace plots. The posterior probability $P(p_{glyco} > p_{non-glyco})$ was computed from posterior samples to quantify the evidence that glycosylation increases the likelihood of POPC lipids traversing the membrane.

4.10 | Cell lines and culture

Immortalized human embryonic kidney cells (HEK293) cell line were obtained from the American Type Culture Collection (ATCC, ref. CRL-1573). ATG9A KO HEK293 cell line was obtained from Richard Youle's lab. Cells were grown in Dulbecco's modified Eagle's medium (DMEM) high glucose (Gibco #31966-021) supplemented with 10% fetal bovine serum (Gibco #10270-106). Cell lines were grown at 37°C in a humidified incubator containing 5% CO_2.

4.11 | Plasmid and DNA transfection

V5-ATG9A plasmid was generated by insertion of human ATG9A sequence into a V5-TurboID-NES pCDNA3 plasmid (Addgene #107169) C-terminal to the V5-tag using the NEBuilder HiFi DNA Assembly Cloning Kit (New England Biolabs (NEB), #E5520S) according to the user guidelines. Subsequently, the sequence encoding TurboID-NES was deleted by mutagenesis using the Platinum SuperFi II DNA Polymerase system (Thermo Scientific #12361010). ATG9A mutants (N99D and N99A) were generated by site-directed mutagenesis using the Platinum SuperFi II DNA Polymerase system and confirmed by sequencing (Eurofins). The cells were transfected with DNA using polyethylenimine (PEI) (PolySciences, #23966-100) in OptiMEM (ThermoFisher) according to the manufacturer guidelines. Oligonucleotides used in this study were obtained from TAG Copenhagen and their sequences are listed in Table S3. The DNA sequence of V5-ATG9A is listed in Table S4.

4.12 | Antibodies

Rabbit ATG9A (Cell Signaling Technology, #13509), rabbit LC3B (Cell Signaling Technology, #2775), mouse beta Actin (C4) (Santa Cruz Biotechnology, #sc-47778), rabbit SQSTM1/p62 (MBL, #PM045).

4.13 | Starvation assay

Cells were seeded in 6 cm plates at 3×10^5 cells/mL. 24 h post transfection the cells were washed twice in Earle's Balanced Salt Solution (EBSS; Sigma-Aldrich, E2888) medium and then incubated in EBSS medium for 4 h with or without 200 nM Bafilomycin A1. Cells were washed three times in PBS before being transferred to 350 μL RIPA lysis buffer (50 mM Tris–HCl pH 7.4, 150 mM NaCl, 0.1% SDS, 0.5% sodium deoxycholate, 1% Triton X-100, 5 mM EDTA) containing protease inhibitor cocktail, NaV, NaF, and β-glycerophosphate, using a cell scraper. Lysis was performed by incubating cells on ice for 30 min. The lysate was centrifuged at 15.000×g for 15 min at 4°C and the supernatant was transferred to a new tube. The protein concentration was determined using the DC protein assay (BioRad).

4.14 | Western blot

Samples for western blots were mixed with NuPAGE SDS-loading buffer and NuPAGE reducing agent. Samples were incubated at 65°C for 15 min prior to separation by electrophoresis using a 15% SDS polyacrylamide gel and subsequently electro transferred to a nitrocellulose membrane (BioRad). The membrane was blocked by incubation in PBS-T (DPBS, 0.1% Tween-20) containing 5% (w/v) nonfat dry milk powder for 1 h. The membrane was incubated in primary antibody (1:1000 dilution) for 1 h at room temperature or overnight at 4°C. The membrane was washed 5 times for 5 min with PBS-T to remove unbound primary antibody and incubated for 1 h at room temperature with the corresponding horseradish peroxidase-conjugated secondary antibody (Goat Anti-rabbit, #1706515 or Anti-mouse, 1706516, IgG (H + L)-HRP Conjugate Bio-Rad) at a 1:3000 dilution. The membrane was subsequently washed five times for 5 min to remove unbound antibodies in PBS-T. The membranes were developed using chemiluminescence (Amersham™ ECL Select™ Western Blotting Detection Reagent, Cytiva) and images were acquired using a ChemiDoc™ Imaging system, Bio-Rad.

To normalize for protein loading, the membrane has been incubated with a mouse monoclonal anti β-actin antibody (Santa Cruz Biotechnology, #sc-47,778). Relative band intensities were determined using the ImageLab software (Bio-Rad). To account for variations in basal LC3-II and SQSTM1/p62 levels under steady-state conditions, autophagy flux was quantified using specific normalization ratios. The synthesis ratio was calculated by comparing the levels of selected autophagy markers in the presence of both an autophagy inducer and a degradation inhibitor to their levels with the inhibitor alone, representing the rate of autophagosome formation. The degradation ratio was determined by comparing marker levels when both the inducer and inhibitor were applied to their levels with the inducer alone, providing a measure of autophagosome turnover.

4.15 | Immunofluorescence

ATG9A-knockout HEK293 or HEK293T cells (5 × 10^5) were seeded on 10-mm glass coverslips and transfected with either wild-type ATG9A or the mutant constructs N99A and N99D. Cells were fixed and permeabilized by incubation in cold methanol (−20°C) for 10 min and subsequently washed three times with PBS. After fixation, cells were blocked for 30 min in 3% BSA in PBS and then incubated overnight at 4°C with a rabbit anti-LC3B antibody (1:200). Following three washes in PBS, cells were incubated for 1 h at room temperature with an Alexa Fluor–conjugated goat anti-rabbit secondary antibody (1:400). Nuclei were stained with Hoechst 33342 (1:1000 in PBS, 10 min) followed by three washes in PBS. Coverslips were mounted on microscope slides using DAKO Fluorescence Mounting Medium and allowed to cure at room temperature before imaging. Images were acquired on a Confocal Microscope Zeiss LSM700.

4.16 | Vesicle size analysis

The images were quantified using the default 'Analyze particles' in ImageJ as described in Runwal et al. (2019). Fluorescence images of LC3B immunostaining were analyzed using ImageJ/Fiji (version: 2.16.0/1.54p). For each image, the LC3B channel was converted to 16-bit and then thresholded using the Otsu algorithm, converted to binary masks. Vesicles were quantified using the Analyze Particles function in ImageJ, with circularity set to 0.20–1.00 and the Exclude on edges option enabled. All thresholding and analysis parameters were kept constant across experimental groups. Vesicle size was first averaged per cell, and these values were then averaged across the analyzed cells for each condition.

4.17 | Statistical analysis

All statistical analyses were performed using GraphPad Prism 10 and R (version 4.5.1) with standard libraries. Unless otherwise indicated, data are presented as mean ± SD. For the autophagy flux assay, we performed Welch's unequal variances *t*-test, while for the vesicle size analyses we used an unpaired *t*-test. Assumptions of normality were verified using Shapiro–Wilk tests; if violated, the Mann–Whitney *U* test was used. Sample sizes (*n*) and exact statistical tests are reported in the figure legends. For computational results (e.g., lipid insertion counts, conformational clusters), averages and standard deviations were calculated from three independent 1 μs replicates. Statistical comparisons were carried out using the same framework as above. For lipid translocation analysis, we used a Bayesian binomial model implemented in Stan via CmdStanR (see Bayesian analysis subsection). Posterior distributions were obtained via MCMC sampling and reported as posterior probabilities for one condition exceeding the other.

AUTHOR CONTRIBUTIONS

Mattia Utichi: Data curation; formal analysis; investigation; methodology; validation; visualization; writing – original draft; writing – review and editing. **Matteo Lambrughi:** Conceptualization; data curation; formal analysis; investigation; methodology; supervision; validation; visualization; writing – original draft. **Henri-Baptiste-Marjault:** Formal analysis; methodology; writing – review and editing. **Christian B. Borg:** Methodology. **Sergio Esteban Echeverría:** Formal analysis; methodology. **Kenji Maeda:** Methodology; writing – review and editing. **Nicholas M. I. Taylor:** Methodology; writing – review and editing. **Anders Gorm Pedersen:** Writing – review and editing; formal analysis; methodology. **Elisa Fadda:** Methodology; writing – review and editing. **Marja Jäättelä:** Funding acquisition; methodology; resources; writing – review and editing. **Elena Papaleo:** Conceptualization; funding acquisition; investigation; project administration; resources; supervision; writing – original draft; writing – review and editing.

CONFLICT OF INTEREST STATEMENT

No potential conflict of interest was reported by the authors.

DATA AVAILABILITY STATEMENT

All data, including input files and simulation trajectories, is freely available on OSF (https://osf.io/c4aqu/).

DECLARATION OF GENERATIVE AI AND AI-ASSISTED TECHNOLOGIES IN THE WRITING PROCESS

During the preparation of this work the author(s) used OpenAI ChatGPT 3.5 to improve the language of the manuscript. After using this service, the authors reviewed and edited the content as needed and took full responsibility for the content of the published article.

ORCID

Nicholas M. I. Taylor https://orcid.org/0000-0003-0761-4921

REFERENCES

Abraham MJ, Murtola T, Schulz R, Páll S, Smith JC, Hess B, et al. GROMACS: High performance molecular simulations through multi-level parallelism from laptops to supercomputers. SoftwX. 2015;2:19–25. https://doi.org/10.1016/j.softx.2015.06.001

Anandakrishnan R, Aguilar B, Onufriev AV. H++ 3.0: automating pK prediction and the preparation of biomolecular structures for atomistic molecular modeling and simulations. Nucleic Acids Research. 2012;40:W537–41. https://doi.org/10.1093/nar/gks375

Bejarano E, Cuervo AM. Chaperone-mediated autophagy. Proceedings of the American Thoracic Society. 2010;7(1):29–39. https://doi.org/10.1513/pats.200909-102JS

Broadbent DG, Barnaba C, Perez GI, Schmidt JC. Quantitative analysis of autophagy reveals the role of ATG9 and ATG2 in autophagosome formation. The Journal of Cell Biology. 2023;222(7):e202210078. https://doi.org/10.1083/JCB.202210078

Chau TH, Chernykh A, Kawahara R, Thaysen-Andersen M. Critical considerations in N-glycoproteomics. Current Opinion in Chemical Biology. 2023;73:102272. https://doi.org/10.1016/j.cbpa.2023.102272

Cheng J, Novati G, Pan J, Bycroft C, Žemgulytė A, Applebaum T, et al. Accurate proteome-wide missense variant effect prediction with AlphaMissense. Science (New York, NY). 2023;381(6664):eadg7492. https://doi.org/10.1126/science.adg7492

Chiduza GN, Garza-Garcia A, Almacellas E, de Tito S, Pye VE, van Vliet AR, et al. ATG9B is a tissue-specific homotrimeric lipid scramblase that can compensate for ATG9A. Autophagy. 2024;20(3):557–76. https://doi.org/10.1080/15548627.2023.2275905

Chovancova E, Pavelka A, Benes P, Strnad O, Brezovsky J, Kozlikova B, et al. CAVER 3.0: a tool for the analysis of transport pathways in dynamic protein structures. PLoS Computational Biology. 2012;8(10):e1002708. https://doi.org/10.1371/journal.pcbi.1002708

Chumpen Ramirez S, Gómez-Sánchez R, Verlhac P, Hardenberg R, Margheritis E, Cosentino K, et al. Atg9 interactions via its

transmembrane domains are required for phagophore expansion during autophagy. Autophagy. 2023;19(5):1459–78. https://doi.org/10.1080/15548627.2022.2136340

Degn K, Beltrame L, Dahl Hede F, Sora V, Nicolaci V, Vabistsevits M, et al. Cancer-related mutations with local or long-range effects on an allosteric loop of p53. Journal of Molecular Biology. 2022; 434(17):167663. https://doi.org/10.1016/J.JMB.2022.167663

Di Rita A, Peschiaroli A, D'Acunzo P, Strobbe D, Hu Z, Gruber J, et al. HUWE1 E3 ligase promotes PINK1/PARKIN-independent mitophagy by regulating AMBRA1 activation via IKKα. Nature Communications. 2018;9:3755. https://doi.org/10.1038/s41467-018-05722-3

Dong GQ, Fan H, Schneidman-Duhovny D, Webb B, Sali A, Tramontano A. Optimized atomic statistical potentials: assessment of protein interfaces and loops. Bioinformatics. 2013; 29(24):3158–66. https://doi.org/10.1093/bioinformatics/btt560

Eskelinen E-L, Tanaka Y, Saftig P. At the acidic edge: emerging functions for lysosomal membrane proteins. Trends in Cell Biology. 2003; 13(3):137–45. https://doi.org/10.1016/S0962-8924(03)00005-9

Eswar N, Webb B, Marti-Renom MA, Madhusudhan MS, Eramian D, Shen M-Y, et al. Comparative protein structure modeling using MODELLER. j/Editorial Board, John E. Coligan (et al.), Chapter 2, Unit 2.9. 2007 https://doi.org/10.1002/0471140864.ps0209s50

Fadda E. Molecular simulations of complex carbohydrates and glycoconjugates. Current Opinion in Chemical Biology. 2022;69: 102175. https://doi.org/10.1016/j.cbpa.2022.102175

Gabry J, Češnovar R, Johnson A, Bronder S. cmdstanr: R Interface to 'CmdStan'. R package version 0.9.0.9000. 2025.

Germain M, Nguyen AP, Le Grand JN, Arbour N, Vanderluit JL, Park DS, et al. MCL-1 is a stress sensor that regulates autophagy in a developmentally regulated manner. The EMBO Journal. 2011;30(2):395–407. https://doi.org/10.1038/EMBOJ.2010.327/SUPPL_FILE/EMBJ2010327.REVIEWER_COMMENTS.PDF

Guardia CM, Tan XF, Lian T, Rana MS, Zhou W, Christenson ET, et al. Structure of human ATG9A, the only transmembrane protein of the Core autophagy machinery. Cell Reports. 2020; 31(13):107837. https://doi.org/10.1016/j.celrep.2020.107837

Gudmundsson S, Singer-Berk M, Watts NA, Phu W, Goodrich JK, Solomonson M, et al. Variant interpretation using population databases: lessons from gnomAD. Human Mutation. 2022; 43(8):1012–30. https://doi.org/10.1002/humu.24309

He S, Ni D, Ma B, Lee JH, Zhang T, Ghozalli I, et al. PtdIns(3)P-bound UVRAG coordinates Golgi-ER retrograde and Atg9 transport by differential interactions with the ER tether and the beclin 1 complex. Nature Cell Biology. 2013;15(10):1206–19. https://doi.org/10.1038/ncb2848

Hess B, Bekker H, Berendsen HJC, Fraaije JGEM. LINCS: a linear constraint solver for molecular simulations. Journal of Computational Chemistry. 1997;18(12):1463–72. https://doi.org/10.1002/(SICI)1096-987X(199709)18:12<1463::AID-JCC4>3.0.CO;2-H

Heyer LJ, Kruglyak S, Yooseph S. Exploring expression data: identification and analysis of Coexpressed genes. Genome Research. 1999;9(11):1106–15. https://doi.org/10.1101/gr.9.11.1106

Huang J, Rauscher S, Nawrocki G, Ran T, Feig M, de Groot BL, et al. CHARMM36m: an improved force field for folded and intrinsically disordered proteins. Nature Methods. 2017;14(1):71–3. https://doi.org/10.1038/nmeth.4067

Javed R, Mari M, Trosdal E, Duque T, Paddar MA, Allers L, et al. ATG9A facilitates the closure of mammalian autophagosomes. The Journal of Cell Biology. 2025;224(2):e202404047. https://doi.org/10.1083/JCB.202404047

Jo S, Kim T, Iyer VG, Im W. CHARMM-GUI: a web-based graphical user interface for CHARMM. Journal of Computational Chemistry. 2008;29(11):1859–65. https://doi.org/10.1002/jcc.20945

Jubb HC, Higueruelo AP, Ochoa-Montaño B, Pitt WR, Ascher DB, Blundell TL. Arpeggio: a web server for calculating and Visualising interatomic interactions in protein structures. Journal of Molecular Biology. 2017;429(3):365–71. https://doi.org/10.1016/j.jmb.2016.12.004

Kishi-Itakura C, Koyama-Honda I, Itakura E, Mizushima N. Ultrastructural analysis of autophagosome organization using mammalian autophagy-deficient cells. Journal of Cell Science. 2014;127: 4089–102. https://doi.org/10.1242/jcs.156034

Klauda JB, Venable RM, Freites JA, O'Connor JW, Tobias DJ, Mondragon-Ramirez C, et al. Update of the CHARMM all-atom additive force Field for lipids: validation on six lipid types. The Journal of Physical Chemistry. B. 2010;114(23):7830–43. https://doi.org/10.1021/jp101759q

Klionsky DJ, Abdel-Aziz AK, Abdelfatah S, Abdellatif M, Abdoli A, Abel S, et al. Guidelines for the use and interpretation of assays for monitoring autophagy (4th edition)1. Autophagy. 2021;17(1): 1–382. https://doi.org/10.1080/15548627.2020.1797280

Kodigepalli KM, Bowers K, Sharp A, Nanjundan M. Roles and regulation of phospholipid scramblases. FEBS Letters. 2015;589(1):3–14. https://doi.org/10.1016/J.FEBSLET.2014.11.036

Kotani T, Kirisako H, Koizumi M, Ohsumi Y, Nakatogawa H. The Atg2-Atg18 complex tethers pre-autophagosomal membranes to the endoplasmic reticulum for autophagosome formation. Proceedings of the National Academy of Sciences. 2018;115(41): 10363–8. https://doi.org/10.1073/pnas.1806727115

Lambrughi M, Sanader Maršić Ž, Saez-Jimenez V, Mapelli V, Olsson L, Papaleo E. Conformational gating in ammonia lyases. Biochimica et Biophysica Acta - General Subjects. 2020; 1864(7):129605. https://doi.org/10.1016/j.bbagen.2020.129605

Landrum MJ, Chitipiralla S, Brown GR, Chen C, Gu B, Hart J, et al. ClinVar: improvements to accessing data. Nucleic Acids Research. 2020;48(D1):D835–44. https://doi.org/10.1093/NAR/GKZ972

Lee J, Cheng X, Swails JM, Yeom MS, Eastman PK, Lemkul JA, et al. CHARMM-GUI input generator for NAMD, GROMACS, AMBER, OpenMM, and CHARMM/OpenMM simulations using the CHARMM36 additive force Field. Journal of Chemical Theory and Computation. 2016;12(1):405–13. https://doi.org/10.1021/acs.jctc.5b00935

Lee J, Patel DS, Ståhle J, Park SJ, Kern NR, Kim S, et al. CHARMM-GUI membrane builder for complex biological membrane simulations with glycolipids and lipoglycans. Journal of Chemical Theory and Computation. 2019;15(1):775–86. https://doi.org/10.1021/acs.jctc.8b01066

Li L, Tong M, Fu Y, Chen F, Zhang S, Chen H, et al. Lipids and membrane-associated proteins in autophagy. Protein & Cell. 2021;12(7):520–44. https://doi.org/10.1007/s13238-020-00793-9

Liu C, Luo J. Protein oligomer engineering: a new frontier for studying protein structure, function, and toxicity. Angewandte Chemie International Edition. 2023;62(23):e202216480. https://doi.org/10.1002/ANIE.202216480

Lomize MA, Pogozheva ID, Joo H, Mosberg HI, Lomize AL. OPM database and PPM web server: resources for positioning of proteins in membranes. Nucleic Acids Research. 2012;40(D1): D370–6. https://doi.org/10.1093/nar/gkr703

MacKerell AD, Bashford D, Dunbrack RL, Evanseck JD, Field MJ, Fischer S, et al. All-atom empirical potential for molecular modeling and dynamics studies of proteins. The Journal of Physical Chemistry. B. 1998;102(18):3586–616. https://doi.org/10.1021/jp973084f

Maeda S, Otomo C, Otomo T. The autophagic membrane tether ATG2A transfers lipids between membranes. Elife. 2019;8: e45777. https://doi.org/10.7554/eLife.45777

Maeda S, Yamamoto H, Kinch LN, Garza CM, Takahashi S, Otomo C, et al. Structure, lipid scrambling activity and role in autophagosome formation of ATG9A. Nature Structural & Molecular Biology. 2020;27(12):1194–201. https://doi.org/10.1038/s41594-020-00520-2

Mäeots ME, Enchev RI. Structural dynamics: review of time-resolved cryo-EM. Acta Crystallographica Section D, Structural Biology. 2022;78(Pt 8):927–35. https://doi.org/10.1107/S2059798322006155

Manak M, Zemek M, Szkandera J, Kolingerova I, Papaleo E, Lambrughi M. Hybrid Voronoi diagrams, their computation and reduction for applications in computational biochemistry. Journal

of Molecular Graphics and Modelling. 2017;74:225–33. https://doi.org/10.1016/j.jmgm.2017.03.018
Matoba K, Kotani T, Tsutsumi A, Tsuji T, Mori T, Noshiro D, et al. Atg9 is a lipid scramblase that mediates autophagosomal membrane expansion. Nature Structural & Molecular Biology. 2020;27(12):1185–93. https://doi.org/10.1038/s41594-020-00518-w
Matoba K, Noda NN. Secret of Atg9: lipid scramblase activity drives de novo autophagosome biogenesis. Cell Death and Differentiation. 2020;27(12):3386–8. https://doi.org/10.1038/s41418-020-00663-1
Mercadante D, Gräter F, Daday C. CONAN: a tool to decode dynamical information from molecular interaction maps. Biophysical Journal. 2018;114(6):1267–73. https://doi.org/10.1016/j.bpj.2018.01.033
Michaud-Agrawal N, Denning EJ, Woolf TB, Beckstein O. MDAnalysis: a toolkit for the analysis of molecular dynamics simulations. Journal of Computational Chemistry. 2011;32(10):2319–27. https://doi.org/10.1002/jcc.21787
Mizushima N, Yoshimori T. How to interpret LC3 immunoblotting. Autophagy. 2007;3(6):542–5. https://doi.org/10.4161/AUTO.4600
Noda NN, Ohsumi Y, Inagaki F. ATG systems from the protein structural point of view ATG systems from the protein structural point of view. 2009;109:1587–98. https://doi.org/10.1021/cr800459r
Nosé S. A molecular dynamics method for simulations in the canonical ensemble. Molecular Physics. 1984;52(2):255–68. https://doi.org/10.1080/00268978400101201
Olivas TJ, Wu Y, Yu S, Luan L, Choi P, Guinn ED, et al. ATG9 vesicles comprise the seed membrane of mammalian autophagosomes. The Journal of Cell Biology. 2023;222(7):e202208088. https://doi.org/10.1083/jcb.202208088
Olsson MHM, Søndergaard CR, Rostkowski M, Jensen JH. PROPKA3: consistent treatment of internal and surface residues in empirical pKa predictions. Journal of Chemical Theory and Computation. 2011;7(2):525–37. https://doi.org/10.1021/ct100578z
Orsi a, Razi M, Dooley HC, Robinson D, Weston a E, Collinson LM, et al. Dynamic and transient interactions of Atg9 with autophagosomes, but not membrane integration, are required for autophagy. Molecular Biology of the Cell. 2012;23(10):1860–73. https://doi.org/10.1091/mbc.E11-09-0746
Parrinello M, Rahman A. Polymorphic transitions in single crystals: a new molecular dynamics method. Journal of Applied Physics. 1981;52(12):7182–90. https://doi.org/10.1063/1.328693
Petersen HG. Accuracy and efficiency of the particle mesh Ewald method. The Journal of Chemical Physics. 1995;103(9):3668–79. https://doi.org/10.1063/1.470043
Popovic D, Dikic I. TBC1D5 and the AP2 complex regulate ATG9 trafficking and initiation of autophagy. EMBO Reports. 2014;15(4):392–401. https://doi.org/10.1002/embr.201337995
Posit Team. RStudio: Integrated Development Environment for R. Posit Software, PBC, Boston, MA. 2025.
Puri C, Renna M, Bento CF, Moreau K, Rubinsztein DC. Diverse autophagosome membrane sources coalesce in recycling endosomes. Cell. 2013;154(6):1285–99. https://doi.org/10.1016/j.cell.2013.08.044
R Core Team. R: a language and environment for statistical computing R Foundation for Statistical Computing Vienna, Austria. 2025.
Reggiori F, Gabius HJ, Aureli M, Römer W, Sonnino S, Eskelinen EL. Glycans in autophagy, endocytosis and lysosomal functions. Glycoconjugate Journal. 2021;38:625–47. https://doi.org/10.1007/s10719-021-10007-x
Reily C, Stewart TJ, Renfrow MB, Novak J. Glycosylation in health and disease. Nature Reviews. Nephrology. 2019;15:346–66. https://doi.org/10.1038/s41581-019-0129-4
Runwal G, Stamatakou E, Siddiqi FH, Puri C, Zhu Y, Rubinsztein DC. LC3-positive structures are prominent in autophagy-deficient cells. Scientific Reports. 2019;9:10147. https://doi.org/10.1038/s41598-019-46657-z
Sawa-Makarska J, Baumann V, Coudevylle N, von Bülow S, Nogellova V, Abert C, et al. Reconstitution of autophagosome nucleation defines Atg9 vesicles as seeds for membrane formation. Science. 2020;369(6508):eaaz7714. https://doi.org/10.1126/science.aaz7714
Schmitt D, Bozkurt S, Henning-Domres P, Huesmann H, Eimer S, Bindila L, et al. Lipid and protein content profiling of isolated native autophagic vesicles. EMBO Reports. 2022;23(12):e53065. https://doi.org/10.15252/embr.202153065
Scrima S, Tiberti M, Campo A, Corcelle-Termeau E, Judith D, Foged MM, et al. Unraveling membrane properties at the organelle-level with LipidDyn. Computational and Structural Biotechnology Journal. 2022;20:3604–14. https://doi.org/10.1016/j.csbj.2022.06.054
Stan Development Team. Stan Reference Manual, Version 2.32.2. 2025.
Staudt C, Gilis F, Boonen M, Jadot M. Molecular determinants that mediate the sorting of human ATG9A from the endoplasmic reticulum. Biochimica et Biophysica Acta (BBA). 2016;1863:2299–310. https://doi.org/10.1016/j.bbamcr.2016.06.007
Takahashi Y, Meyerkord CL, Hori T, Runkle K, Fox TE, Kester M, et al. Bif-1 regulates Atg9 trafficking by mediating the fission of Golgi membranes during autophagy. Autophagy. 2011;7(1):61–73. https://doi.org/10.4161/auto.7.1.14015
Tang Z, Takahashi Y, He H, Hattori T, Chen C, Liang X, et al. TOM40 targets Atg2 to mitochondria-associated ER membranes for phagophore expansion. Cell Reports. 2019;28(7):1744–1757.e5. https://doi.org/10.1016/j.celrep.2019.07.036
Tanida I, Minematsu-Ikeguchi N, Ueno T, Kominami E. Lysosomal turnover, but not a cellular level, of endogenous LC3 is a marker for autophagy. Autophagy. 2005;1(2):84–91. https://doi.org/10.4161/AUTO.1.2.1697
Umeki N, Hirose K, Uyeda TQP. Cofilin-induced cooperative conformational changes of actin subunits revealed using cofilin-actin fusion protein. Scientific Reports. 2016;6(1):1–13. https://doi.org/10.1038/srep20406
Valverde DP, Yu S, Boggavarapu V, Kumar N, Lees JA, Walz T, et al. ATG2 transports lipids to promote autophagosome biogenesis. The Journal of Cell Biology. 2019;218(6):1787–98. https://doi.org/10.1083/JCB.201811139
van Vliet AR, Chiduza GN, Maslen SL, Pye VE, Joshi D, de Tito S, et al. ATG9A and ATG2A form a heteromeric complex essential for autophagosome formation. Molecular Cell. 2022;82(22):4324–4339.e8. https://doi.org/10.1016/j.molcel.2022.10.017
Varki A. Biological roles of glycans. Glycobiology. 2017;27(1):3–49. https://doi.org/10.1093/GLYCOB/CWW086
Wang Y, Dahmane S, Ti R, Mai X, Zhu L, Carlson LA, et al. Structural basis for lipid transfer by the ATG2A–ATG9A complex. Nature Structural & Molecular Biology. 2024;32(1):35–47. https://doi.org/10.1038/s41594-024-01376-6
Yamamoto H, Zhang S, Mizushima N. Autophagy genes in biology and disease. Nature Reviews. Genetics. 2023;24:382–400. https://doi.org/10.1038/s41576-022-00562-w
Young ARJ, Chan EYW, Hu XW, Köchl R, Crawshaw SG, High S, et al. Starvation and ULK1-dependent cycling of mammalian Atg9 between the TGN and endosomes. Journal of Cell Science. 2006;119(Pt 18):3888–900. https://doi.org/10.1242/jcs.03172

SUPPORTING INFORMATION

Additional supporting information can be found online in the Supporting Information section at the end of this article.

How to cite this article: Utichi M, Lambrughi M, Marjault H-B, Borg CB, Echeverría SE, Maeda K, et al. Role of *N*-glycosylation as a determinant of ATG9A conformations and activity. Protein Science. 2026;35(1):e70390. https://doi.org/10.1002/pro.70390